11-1-2023

The Effect of a Mn(III)Tetrakis(4-Benzoic Acid)Porphyrin (Mntbap) Coating on he Chronic Recording Performance of Planar Silicon Intracortical Microelectrode Arrays

George F. Hoeferlin
Case Western Reserve University, gfh16@case.edu

Lindsey N. Druschel
Case Western Reserve University, lnd24@case.edu

Olivia K. Krebs
Case Western Reserve University, oxk72@case.edu

Dhariyat M. Menendez
Case Western Reserve University, dmm194@case.edu

Jonathan L. Duncan
Case Western Reserve University, jld155@case.edu

Recommended Citation

Ana G. Hernandez-Reynoso, Brandon S. Sturgill, George F. Hoeferlin, Lindsey N. Druschel, Olivia K. Krebs, Dhariyat M. Menendez, Teresa T.D. Thai, Thomas J. Smith, Jonathan Duncan, Jichu Zhang, Gaurav Mittal, Rahul Radhakrishna, Mrudang Spandan Desai, Stuart F. Cogan, Joseph J. Pancrazio, Jeffrey R. Capadona. The effect of a Mn(III)tetrakis(4-benzoic acid)porphyrin (MnTBAP) coating on the chronic recording performance of planar silicon intracortical microelectrode arrays. Biomaterials, Volume 303, 2023, 122351. https://doi.org/10.1016/j.biomaterials.2023.122351

Biomaterials 303 (2023) 122351

Contents lists available at ScienceDirect

Biomaterials

journal homepage: www.elsevier.com/locate/biomaterials

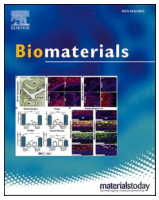

The effect of a Mn(III)tetrakis(4-benzoic acid)porphyrin (MnTBAP) coating on the chronic recording performance of planar silicon intracortical microelectrode arrays

Ana G. Hernandez-Reynoso [a], Brandon S. Sturgill [a], George F. Hoeferlin [b,c], Lindsey N. Druschel [b,c], Olivia K. Krebs [b,c], Dhariyat M. Menendez [b,c], Teresa T.D. Thai [a], Thomas J. Smith [d], Jonathan Duncan [b,c], Jichu Zhang [b,c], Gaurav Mittal [b,c], Rahul Radhakrishna [a], Mrudang Spandan Desai [a], Stuart F. Cogan [a], Joseph J. Pancrazio [a,**], Jeffrey R. Capadona [b,c,*]

[a] Department of Bioengineering, The University of Texas at Dallas, 800 W Campbell Rd, Richardson, TX, 75080, United States
[b] Department of Biomedical Engineering, Case Western Reserve University, 10900 Euclid Ave, Cleveland, OH, 44106, United States
[c] Advanced Platform Technology Center, Louis Stokes Cleveland Veterans Affairs Medical Center, 10701 East Blvd, Cleveland, OH, 44106, United States
[d] School of Behavioral and Brain Sciences, The University of Texas at Dallas, 800 W Campbell Rd, Richardson, TX, 75080, United States

ARTICLE INFO

Keywords:
Intracortical microelectrodes$_1$
Recording neural interfaces$_2$
neuroinflammation$_3$
Oxidative stress$_4$
MnTBAP coating$_5$

ABSTRACT

Intracortical microelectrode arrays (MEAs) are used to record neural activity. However, their implantation initiates a neuroinflammatory cascade, involving the accumulation of reactive oxygen species, leading to interface failure. Here, we coated commercially-available MEAs with Mn(III)tetrakis(4-benzoic acid)porphyrin (MnTBAP), to mitigate oxidative stress. First, we assessed the *in vitro* cytotoxicity of modified sample substrates. Then, we implanted 36 rats with uncoated, MnTBAP-coated ("Coated"), or (3-Aminopropyl)triethoxysilane (APTES)-coated devices – an intermediate step in the coating process. We assessed electrode performance during the acute (1–5 weeks), sub-chronic (6–11 weeks), and chronic (12–16 weeks) phases after implantation. Three subsets of animals were euthanized at different time points to assess the acute, sub-chronic and chronic immunohistological responses. Results showed that MnTBAP coatings were not cytotoxic *in vitro,* and their implantation *in vivo* improved the proportion of electrodes during the sub-chronic and chronic phases; APTES coatings resulted in failure of the neural interface during the chronic phase. In addition, MnTBAP coatings improved the quality of the signal throughout the study and reduced the neuroinflammatory response around the implant as early as two weeks, an effect that remained consistent for months post-implantation. Together, these results suggest that MnTBAP coatings are a potentially useful modification to improve MEA reliability.

1. Introduction

Intracortical microelectrode arrays (MEAs) implanted in the motor cortex can record neural activity associated with voluntary movement. Because of this, MEAs have been widely used to develop brain-machine interfaces, restoring lost function in paralyzed and injured individuals [1–7]. In addition, these devices have been useful in advancing the understanding of brain circuitry and cortical mapping in healthy and diseased states [8–10]. However, implantation of MEAs into the brain results in displacement and mechanical tearing of brain tissue, rupture of the blood-brain barrier with infiltration of macrophages, and initiation of the neuroinflammatory cascade [11–15]. This process is

* Corresponding author. 2071 Martin Luther King Jr, DriveRoom 509, Cleveland, OH, 44106, United States
** Corresponding author. 800 W. Campbell Rd, AD 3.202, Richardson, TX, 75080, United States.
E-mail addresses: ana.hernandezreynoso@utdallas.edu (A.G. Hernandez-Reynoso), brandon.sturgill@utdallas.edu (B.S. Sturgill), gfh16@case.edu (G.F. Hoeferlin), lnd24@case.edu (L.N. Druschel), oxk72@case.edu (O.K. Krebs), dmm194@case.edu (D.M. Menendez), teresa.thai@utdallas.edu (T.T.D. Thai), thomas.smith2@utdallas.edu (T.J. Smith), jld155@case.edu (J. Duncan), jxz1011@case.edu (J. Zhang), gxm319@case.edu (G. Mittal), radhakrishnar@utdallas.edu (R. Radhakrishna), mrudang.desai@utdallas.edu (M.S. Desai), stuart.cogan@utdallas.edu (S.F. Cogan), joseph.pancrazio@utdallas.edu (J.J. Pancrazio), jrc35@case.edu (J.R. Capadona).

https://doi.org/10.1016/j.biomaterials.2023.122351
Received 9 August 2022; Received in revised form 27 September 2023; Accepted 11 October 2023
Available online 1 November 2023

characterized by the activation of microglial cells that migrate to the implant site. Activated microglia release inflammatory cytokines that activate and recruit distant astrocytes, forming a glial scar and encapsulating the implanted device. The presence of macrophages, microglia, and activated astrocytes increase the production of reactive oxygen species (ROS) such as hydroxyl, superoxide anion, nitric oxide, and hydrogen peroxide that accumulate around the implant site [16,17]. Furthermore, when the superoxide nitric oxide and superoxide anion combine, they produce toxic peroxynitrate [18]. Previous work has demonstrated that implantation of intracortical MEAs can elicit the accumulation of these ROS around the implant site [16,19,20]. The central nervous system lacks endogenous enzymatic antioxidants to reduce these ROS [21], which can result in oxidization of lipids, proteins, carbohydrates, and nucleotides. The oxidation of these biomolecules can be catastrophic for the fate of oligodendrocytes and neurons, causing interference with myelination, mitochondrial dysfunction, and neuronal loss [22,23]. These processes contribute, at least in part, to failure of the neural interface since the ability of MEAs to record extracellular action potentials is related to the proximity of viable neurons around the implant [24,25]. Substantial efforts have been taken to improve the long-term reliability of recording MEAs post-implantation, including the use of MEA surface coatings, including bioactive compounds. For example, Oakes et al. [26] used extracellular matrix coatings that reduced astrocyte expression around the implant site (within 50 μm), but this modification also increased blood-brain barrier permeability, raising concerns about the impact on recording reliability. Sawyer et al. [27] identified monocyte chemoattractant protein 1 (MCP1) – a switch that changes phenotype expression of macrophages and microglia polarization – as an important protein for the propagation of neuroinflammation at acute and sub-chronic time points. Sawyer et al. showed that pharmacological inhibition of MCP1 improved neuronal survival post-implantation. Cell adhesion molecule L1 [28] has also been used to promote neuronal cell integration to MEAs and a reduction in activation and accumulation of microglia.

Our group has focused on improving the longevity of recording MEAs by attempting to modulate the accumulation of reactive oxygen species around the implant. We have used antioxidants such as resveratrol, curcumin, and dimethyl fumarate delivered either systemically or locally to attenuate the accumulation of ROS around the MEA implant site [29–34]. Short-term administration of these antioxidants has significantly improved neuronal viability; however, these improvements appear to be lost over chronic implantation periods. Because of this, we have developed [35] a coating based on the immobilization of commercial Mn(III)tetrakis(4- benzoic acid)porphyrin (MnTBAP), which is a synthetic metalloporphyrin that has been shown to scavenge ROS, including intracellular superoxide anion and the harmful peroxynitrate [36–40]. We showed *in vitro* that the scavenging effect of the MnTBAP coating on glass surfaces with seeded reactive microglia (BV-2) was active for several days after exposure to physiologically relevant conditions [35]. We recently developed the tools and methodology to achieve surface modifications of planar silicon intracortical MEAs and demonstrated the ability to apply MnTBAP coatings onto functional recording devices [41]. Here, we investigated the effect of the MnTBAP coating on the planar intracortical MEA implant sites and assessed the impact on acute (1–5 weeks), sub-chronic (6–11 weeks), and chronic (12–16 weeks) recording performance *in vivo*. We found that the use of this novel coating reduces the glial scar around the MEA as soon as 2 weeks post-implantation, improving neuronal viability, recording quality, and electrode performance chronically.

2. Materials and methods

2.1. In vitro cell assessment for testing cytotoxicity

Prior to conducting *in vivo* experiments, *in vitro* cytotoxicity testing was completed on MnTBAP-coated samples having undergone disinfecting or sterilization treatment including ethanol disinfection (submerged in 70 % ethanol for 5 min), dry heat (180 °C for 4 h), ethylene oxide sterilization, and autoclave (15 psi at 121 °C for 35 min). *In vitro* assessment followed previously established protocols for the synthesis of glass coverslip samples and MEAs [41], and for direct contact cytotoxicity test [35]. Briefly, glass coverslips were cleaned using a six-step sequence of 5-min rinses comprised of DI water with 1 % Liquinox, deionized water, a second rinse in deionized water, acetone, methanol, and isopropyl alcohol. Glass coverslips were further cleaned using a UV Ozone treatment for 15 min. Following procedures detailed by Ref. [42], the samples were then immediately placed in a vacuum desiccator with liquid (3-Aminopropyl)triethoxysilane (APTES) and a vacuum was pulled to allow for the gas phase deposition of APTES onto the sample surfaces with the modifications detailed in Ref. [41]. The samples remained in the desiccator under vacuum for 24 h, after which the samples were submerged in a solution containing MnTBAP activated via carbodiimide crosslinking chemistry as detailed elsewhere [35]. The glass coverslips were incubated for 18 h at room temperature on a shaker table in the solution containing MnTBAP, and then washed three times alternating deionized water and 95 % EtOH. Adherent cell type (NIH3T3, fibroblasts, ~200 cells/mm^2) [43] and highly aggressive proliferating immortalized cells (HAPI, microglia/macrophages, ~50 cells/mm^2) [44] were seeded on top of the glass coverslips to complete cytotoxicity experiments. We included two uncoated glass coverslips cell viability controls: a negative control with all live cells (uncoated glass coverslip, sterilized with ethylene oxide) and a positive control with all dead cells (uncoated glass coverslip cleaned, sterilized with ethylene oxide and exposed to 70 % methanol for 30 min). Following a 24-h incubation, cell viability was assessed with a LIVE/DEAD® Viability/Cytotoxicity Kit (Life Technologies, Carlsbad, CA, US). Cells were stained by incubating with 8 μM ethidium homodimer (EthD-1) and 0.1 μM calcein-AM in PBS for 15 min. Samples were then imaged using an inverted AxioObserver Z1 (Zeiss, Oberkochen, Germany) equipped with an AxioCam MRm. The percentage of dead cells was calculated as the normalized fluorescence intensity compared to the positive controls.

2.2. MnTBAP coating of MEAs

Multielectrode arrays were coated with MnTBAP as previously described [41] via gas-phase deposition and aqueous solution exposure. Custom 3D-printed tools were used to hold and manipulate MEAs during the entirety of the coating process. Briefly, MEAs were cleaned using a sequential six-step wash consisting of 5-min rinses with deionized water with 1 % Liquinox, 2*x* washes in deionized water, acetone, methanol, and finally isopropyl alcohol. Further cleaning to prepare for APTES coating was done using a UV Ozone cleaner treatment for 15 min. Once clean, the 3D-printed tools loaded with the MEAs were placed inside a vacuum desiccator (25 psi) after adding 400 μL to allow amine functionalization and the process was repeated two times: the first two times, the vacuum was held at 25 psi for 20 min, for the third time it was held at 25 psi for 24 h. Once amine functionalization of the MEA surface was done using APTES, the MEAs were coated with MnTBAP by placing the MEA into a well plate containing functionalized MnTBAP solution on a shaker for 18 h at room temperature. After incubation in MnTBAP, MEAs were dipped in glycine to quench the MnTBAP reaction. The MEAs were then washed using deionized water before being packaged for ethylene oxide (ETO) sterilization.

All coated substrates were immediately stored in desiccators under vacuum once the coatings were assembled. Coated substrates were typically implanted (or used in experiments) within 3–4 weeks of coating. The stability of the coatings under these conditions has been validated via XPS [41].

2.3. Animals and surgical implantation

Three cohorts of adult male Sprague-Dawley rats (N = 36) were used

in this research. The first cohort (N = 3), approved by the Louis Stokes Cleveland Department of Veterans Affairs Medical Center Institutional Animal Care and Use Committee, was used to assess the histological outcomes of the neural tissue surrounding MnTBAP-coated ("Coated") and control uncoated planar silicon non-functional probes ("Uncoated"). The second cohort (N = 24), approved by The University of Texas at Dallas Institutional Animal Care and Use Committee, was used to assess the electrophysiological performance of MnTBAP-coated vs. uncoated 16-channel functional MEAs (A1x16-3-100-177-CM16LP, iridium electrode sites, NeuroNexus Technologies, Ann Arbor, MI, US). The third cohort (N = 9), approved by the Case Western Reserve University Institutional Animal Care and Use Committee, was used to assess the neuroinflammatory response using changes in inflammatory gene expression at 2 weeks (n = 3), 7 weeks (n = 3), or 11 weeks (n = 3) post-implantation. Animals in the first cohort received bilateral implants: one uncoated silicon probe and one MnTBAP-coated silicon probe. Animals in the second cohort were implanted with either an uncoated MEA (n = 8, 128 electrode sites total), an MEA after surface functionalization with the intermediate APTES step described above (n = 7, 112 electrode sites), or an MnTBAP-coated MEA (n = 9, 144 electrode sites). For the third cohort, animals were each implanted with three silicon non-functional probes: one uncoated control, one APTES-coated, and one MnTBAP-coated.

The surgical procedure for all cohorts followed previously established protocols [45–48]. Briefly, animals of both cohorts were anesthetized using vaporized isoflurane (1.8–2.2 %) mixed with medical grade oxygen (500 mL/min; SomnoSuite® for Mice & Rats, Kent Scientific Corporation, Torrington, CT, US). The fur on the scalp around the surgical site was removed for an aseptic surgery and then the animals were transferred onto a stereotaxic frame (David Kopf Instruments, Tujunga, CA, US). Vital signs were monitored throughout the entire duration of the procedure and the temperature was maintained using a far-infrared warming pad (PhysioSuite® for Mice & Rats, Kent Scientific Corporation, Torrington, CT, US). The surgical site was cleaned with alternating betadine and alcohol swabs, followed by a subcutaneous injection of 0.5 % bupivacaine hydrochloride (Marcaine, Hospira, Lake Forest, IL, US) at the incision site. An incision was made at the midline of the scalp and the muscles and connective tissue underneath were removed. Bregma, lambda, and the sagittal suture were located. For the second cohort only, two stainless steel bone screws (#51457, Stoelting Co., Wood Dale, IL, USA) were inserted onto the skull acting as ground and reference for electrophysiological recordings and a third screw was inserted for anchoring (coordinates AP,ML,DV at approximately 2,-2,-1 mm; −2,-2.5 mm,-1; −2,2 mm,-1; and 4,2 mm). Screw holes were made via a micromotor-controlled drill press with foot pedal (P-DP70, Foredom Electrical Company, Blackstone Industries, LLC, Bethel, CT, US) mounted to the stereotaxic arm. A 1 mm × 1 mm craniotomy was made targeting the primary motor cortex (M1), followed by durotomy to allow for MEA insertion. For the third cohort only, craniotomies were made 1.5 mm lateral and 1.0 mm anterior and posterior to the bregma. Implant types were randomly assigned to a different craniotomy site in each animal, with each animal receiving all three implant conditions and a craniotomy only control. Then, MEAs were implanted into a cortical depth of 2 mm using a precision-controlled inserter (NeuralGlider, Actuated Medical, Inc., Ann Arbor, MI, US), avoiding disruption of major surface blood vessels to minimize hemorrhaging [49]. The second cohort additionally received placement of a dural graft around the MEA (Biodesign Dural Graft, Cook Medical, Bloomington, IN, US) to cover the durotomy site, followed by a layer of tissue adhesive (GLUture, World Precision Instruments, Sarasota, FL, US) to seal the craniotomy site. A dental cement headcap was shaped around the implant in order to tether the device to the skull. The incision was then closed using surgical staples and the animals were given 0.05 mL/kg intramuscular cefazolin (Med-Vet International, Mettawa, IL, US) as prophylaxis, and 0.15 mL/kg of subcutaneous slow-release buprenorphine (ZooPharm, LLC., Laramie, WY, US) for pain management every 72 h for 5 days.

In contrast, no screws were implanted for the first cohort, and a MnTBAP-coated non-functional probe (n = 3) was implanted either on the right or left side of the midline (randomly assigned) followed by uncoated non-functional probe (n = 3) implanted contralaterally on a second craniotomy of the same dimensions (following the same procedures described above). There were slight differences in the following medication to comply with IACUC requirements at both institutions. For the first cohort of animals with non-functional devices, meloxicam (0.2 mg/100 g) every 24 h for two days was given instead of buprenorphine. For animals in the second cohort, a sulfamethoxazole and trimethoprin oral suspension (200 mg/40 mg/5 mL, Aurobindo Pharma, Dayton, NJ, US) in their drinking water (1 mL/100 mL drinking water) was given for one-week post-implantation.

2.4. Histological tissue processing

Animals in the first cohort (N = 3) were euthanized 2 weeks post-implantation to assess the acute histological response; all animals in the second cohort were euthanized 16 weeks post-implantation. Euthanasia was performed via an IP injection of ketamine (160 mg/kg) and xylazine (20 mg/kg) to induce anesthesia. Anesthetic depth was monitored via toe pinch and any associated animal movement. Once fully anesthetized, an incision was made vertically along the abdomen, just below the xiphoidal process, to expose the abdominal cavity. A lateral cut was made across the abdominal cavity followed by a vertical cut across the rib cage on both sides. The diaphragm was cut with scissors, and the rib cage held up to expose the pleural cavity and heart. Next, the sternum was clamped with a hemostat to keep the heart exposed along with major blood vessels. A small incision was made at the left ventricle of the heart, and a gavage inserted through the left ventricle into the aorta and clamped to prevent movement. The right atrium was snipped to allow blood and perfused liquid to flow out. The rat was then perfused with 400–500 mL 1*x* phosphate buffered saline (1X PBS, Invitrogen, Calsbad, CA, USA) at 100 mL/min, until the liquid flowing out of the right atrium was clear and the liver flushed to a beige color. Following which, the rat was perfused with 400–500 mL of cold 10 % buffered formalin (Fisher Chemical, Waltham, MA). After complete perfusion, the rat was decapitated, and brain extracted. The brain was then placed in 10 % buffered formalin for 24 h, followed by a serial exchange of sucrose starting with 10 % sucrose (Sucrose from Millipore Sigma, Burlington, MA) solution in 1X PBS for 24 h, then 20 % sucrose solution for 24 h, 30 % sucrose solution for 48 h, and the last exchange was with fresh 30 % sucrose solution until the brains were frozen for sectioning. Following freezing using Optimal Cutting Temperature compound (OCT, Sakura Finetek USA Inc, Torrance, CA, USA, #25608-930), the brain was sliced on a cryostat at 20 μm section thickness and mounted onto microscope slides (SuperFrost Plus, FisherBrand, Hampton, NH) for immunohistochemistry.

The animals in the third cohort (N = 9) were euthanized at 2 weeks post-implantation (n = 3), 7 weeks post-implantation (n = 3), or 11 weeks post-implantation (n = 3) to assess the changes in neuroinflammatory and oxidative stress gene expression using the Nanostring nCounter (MAX/FLEX) Analysis System. The procedures above described for perfusion were followed for this subset of animals except for the administration of formalin, which was replaced by 30 % sucrose in PBS.

2.5. Immunohistochemistry

Standard immunohistochemistry protocols from our lab were utilized for the assessment of activated microglia/macrophages, astrocytes, blood-brain barrier permeability, and neuronal density around the electrode interface for animals from the first and second cohorts [16, 50–52]. For the first cohort, sliced brain tissue was thawed in a humidity chamber at room temperature for 1 h. Tissue was rehydrated with gentle

application of 1xPBS to the tissue and to remove OCT compound. Following which, 1xPBS-0.1%T (1*x* PBS, 0.1 % Triton-X100) was applied to permeabilize the tissue. Tissue was then incubated for 1 h with goat serum blocking buffer (1xPBS, 0.3%Triton-X100, 4 % Goat serum) to block cross-reactivity with secondary antibodies. After blocking buffer incubation, one half of the tissue sections were treated with rabbit anti-immunoglobulin G (IgG, 1:100, Bio-Rad, Hercules, CA, USA, Catalog #618501) to visualize blood-brain barrier permeability [14] and mouse anti-CD68 (CD68, 1:100, Millipore Sigma, Burlington MA, USA, Catalog #MAB1435) to visualize activated microglia and macrophages and incubated overnight at 4 °C. The other half of tissue were incubated overnight at 4 °C with mouse anti-neuronal nuclei (NeuN 1:250, Millipore Sigma, Burlington, MA, USA, Catalog #MAB3477) to visualize neuronal cells and rabbit anti-glial fibrillary acidic protein (GFAP, 1:500, Agilent Dako, Santa Clara, CA, USA, Catalog #Z0334429-2) to visualize astrocytes. The next day, after application of primary antibodies, all the tissue slices were washed with 1xPBS-0.1%T. Subsequently, the tissue was incubated at room temperature for 2 h in secondary antibodies in goat serum blocking buffer. Buffer was made up of fluorescent AlexaFluor secondary antibodies 488/594 (1:1000, Invitrogen, Waltham, MA, USA, Catalog #PIA32723, and #A11037, respectively) to visualize markers along with 4′6-diamidino-2-phenylindole (DAPI) (1:3600, 10.9 mM, Invitrogen, Waltham, MA, USA, Catalog #D3571) to visualize cell nuclei. Following incubation, tissue was then washed with 1xPBS-0.1%T and incubated in copper sulfate buffer (0.5 mM copper sulfate in ammonium acetate for 10 min) to reduce tissue auto fluorescence [53]. Lastly, tissue was washed with dH_2O and excess dH_20 was wiped off before slides were mounted with coverslips using mounting medium (Fluoromount-G, Southern Biotech, Birmingham, AL, USA, Catalog #010001).

For the second cohort, frozen brains were prepared for immunohistochemical staining by first sectioning at 20 μm using a cryostat and placing brain sections on microscope slides (SuperFrost Plus, FisherBrand, Hampton, NH). Brain sections were stored in a −80 °C freezer until staining. Immunohistochemical staining was performed using the Leica Bond RX Automated Stainer (Leica Biosystems, Wetzlar, Germany) and previously established laboratory protocols [52,54–56]. Brain tissue from animals with representative recording performance was stained for astrocyte activity and glial scarring (glial fibrillary acidic protein, GFAP), microglia/macrophage activity (CD68), neuronal nuclei (NeuN), and BBB damage (immunoglobulin-G, IgG). Microscope slides with sectioned brains were first thawed in a humidity chamber for 30 min and washed with 1*x* PBS to remove residual OCT. The tissue was then loaded into the Bond RX staining system. Tissue was first washed with proprietary Bond RX detergent to permeabilize the tissue, followed by a 10-min 80 °C heat-induced epitope retrieval (HIER) step using a proprietary sodium-citrate-based solution. After HIER, one set of tissue was incubated for 30 min with mouse anti-CD68 (CD68, 1:100, Millipore Sigma, Burlington, MA, USA, Catalog #MAB1435) to visualize activated microglia and macrophages and rabbit anti-GFAP (1:500, Agilent Dako, Santa Clara, CA, USA, Catalog #Z0334429-2) for activated astrocytes. The other set of tissue was incubated first for 30 min with rabbit anti-IgG (1:100, Bio-Rad, Hercules, CA, USA, Catalog #618501) to visualize BBB damage, followed by a second 30-min incubation with mouse anti-NeuN (1:250, Millipore Sigma, Burlington, MA, USA, Catalog #MAB3477) to visualize neuron populations. Following primary antibody incubation, both tissue sets were removed from the Bond RX and placed into a humidity chamber. Tissue was then incubated for 2 h at room temperature using a secondary antibody solution consisting of fluorescent AlexaFluor secondary antibodies 488/594 (1:1000, Invitrogen, Waltham, MA, USA, Catalog #D3571) and 4′6-diamidino-2-phenylindole (DAPI) (1:3600, 10.9 mM, Invitrogen, Waltham, MA, USA, Catalog #D3571) suspended in a 1*x* PBS with 0.3 % triton buffer solution. DAPI is used to visualize all cell nuclei. After 2 h, the tissue was washed with dH_2O. Slides were then wiped dry and mounted with coverslips using Fluoromount-G mounting medium (Southern Biotech, Birmingham, AL, USA, Catalog #010001).

2.6. Imaging and analysis

Fluorescent tissue slides for the first cohort were imaged using an Axioscan.Z1 (Zeiss Inc., Oberkochen, Germany) at 20× objective under matching exposure times tailored for each individual fluorescent marker. During immunohistochemical image analysis, exclusions were drawn around artifacts to remove them from analysis. After the intensity of each image was measured, a visual inspection was performed individually on each image file to double check the presence of artifacts or poor staining quality. If such an image persisted through intensity measurement, that image was removed from analysis. Holes from implantation were identified, and images were converted from native.CZI file format to 16-bit.TIFF for processing. A custom MATLAB script for analysis, called SECOND, was used where the implantation hole is outlined and any artifacts are excluded from analysis [57]. Using SECOND, each fluorescent marker was quantified in 50 μm bins expanding in a ring from the center of the identified implantation hole. GFAP, IgG, and CD68 were analyzed up to 500 μm away from the implantation with background intensity defined as the 450–500 μm binning interval to normalize intensity in all other bins. Neurons were automatically quantified via Neurolucida and manually verified using a custom MATLAB program called AfterNeuN up to 400 μm away from the hole [16]. Background neuron density was defined as the 400–450 μm binning interval, and all bins within the 0–400 μm distance were normalized using this background density value.

For the second cohort, once the coverslips were dried and secure, stained tissue was imaged using the 20× objective of a confocal microscope (Nikon A1R HD Multiphoton System, Nikon Instruments Inc., Melville, NY, USA) to qualitatively compare brain tissue health across groups. All images were taken using the same fluorescent exposure and gain across each fluorescent stain.

2.7. Tissue extraction

For animals in the third cohort, brains were removed from the skull immediately after perfusion to prevent excessive RNA degradation. Implants were explanted prior to flash freezing the brains in optimal cutting temperature compound (OCT) and stored at −80 °C until further processing. Cortical brain tissues surrounding the neural probes were cryo-sectioned into 150 μm thick frozen slices. We collected six to seven 150 μm thick sections for RNA isolation.

2.8. RNA isolation

Extracted brain tissue was homogenized as previously described by our lab [52,58–60]. Briefly, we placed pooled samples from an individual animal into 2.0 mL homogenization microtubes prefilled with 1.5 mm zirconium beads (Benchmark scientific D1032-15) and 1 mL Qiazol (RNA extraction lysate). Tissue was homogenized by shaking at 4000 rpm for 1 min on a Bead Bug Homogenizer (Benchmark Scientific D1030). This homogenization allows for RNA isolation.

The RNA was extracted at the Gene Expression and Genotyping Facility at Case Western Reserve University by purifying RNA from the homogenized tissue with standard kits (RNeasy® Plus Universal Mini Kit; Qiagen 73404). RNA quality and quantity were determined using Nanodrop and TapeStation. We concentrated samples with low concentration with a Speedvac.

2.9. Gene expression assay

Here, we used a fluorescent barcode technology developed by NanoString Technologies (Seattle, WA) to determine gene expression by counting individual genes. RNA (~25–100 ng per sample) was hybridized with a codeset containing capture probes and reporter probes that bind to specific genes of interest. Here, we utilized a customized codeset containing 152 genes. The genes were selected based on available

oxidative stress markers, previously analyzed genes upregulated after MEA implantation, and previously identified housekeeping genes for rat brain tissue (Table 1) [52,58–61].

Negative controls and positive controls were spiked in to assess assay efficiency. Samples were incubated at 65 °C for 18 h, loaded onto cartridges, and processed with nCounter® MAX/FLEX Analyzer. Measurements were taken at 280 Field-of-View per sample for maximum resolution, and the relative number of each gene was determined from absolute counts of fluorescent barcode reporters using the nCounter® MAX Analyzer.

2.10. Normalization of gene expression data

RNA expression data was analyzed using the NanoString nSolver software as previously described by our lab [52,58–60]. Briefly, raw expression counts were normalized with positive control probe counts to account for assay efficiency and housekeeping genes that normalize to the amount of RNA collected per sample. Next, a differential expression analysis was performed to determine how gene expression changes with treatment. Any gene with less than 20 counts in 85 % of the samples was removed. The expression ratio was plotted on a log2 scale and called the Log2FoldChange. Expression of Log2FoldChange >1 indicates a two-fold increase, whereas Log2FoldChange < -1 indicates a two-fold decrease. A 2-tailed, unequal variance *t*-test was performed for each

Table 1
Complete list of neuroinflammatory and oxidative stress genes of interest utilized in the study. Here we list the 152 genes examined in rat brain tissue in this study using a combination of custom genes (shown in **green** with light orange shading) and preset genes from NanoString (shown in **black**). Housekeeping genes are highlighted in **red** with light grey shading.

Abl1	*C4A*	*Ddit3*	*GSTA1*	*Ins2*	*Ngfg*	*Prnp*	*SPP1*
Ager	*C5AR1*	*Dnm2*	*Gsta2*	*Ipcef1*	*Ngfr*	*Psen1*	*Src*
Aif1	*Casp3*	*DOCK2*	*GSTM2*	*IRAK4*	*Nme5*	*PSMB8*	*Srxn1*
AIM2	*CASP8*	*Ehd2*	*Gstp1*	*IRF7*	*Nol3*	*Ptgs2*	*Stx2*
Akt1	*CCL1*	*Ep300*	*Gucy1b3*	*ITGAM*	*Nos1*	*PTPN6*	*Tbp*
Apoe	*Ccl5*	*Ercc6*	*H2-T23*	*Jun*	*Nos3*	*PTX3*	*Tnf*
App	*Ccs*	*ERLEC1*	*Hdac2*	*KEAP1*	*Noxa1*	*Rela*	*TNFRSF1A*
ARC	*CD14*	*Fas*	*Hdac6*	*LILRB4A*	*Nqo1*	*Rpl13a*	*TNFRSF25*
Atf4	*CD36*	*FCER1G*	*Hgf*	*Lpo*	*Nr2f6*	*Rps18*	*Tor1a*
Atp13a2	*CD45*	*FCGR2B*	*Hif1a*	*Lrrk2*	*Nr4a2*	*SCD1*	*Tpm1*
Atp7a	*CD68*	*Fn1*	*Hmox1*	*Mapt*	*Osgin1*	*Sdha*	*Trp53*
Atrn	*CD74*	*Fos*	*Hprt*	*Mgmt*	*OSMR*	*SERPINA3N*	*Trpm2*
Bad	*CD84*	*Fxn*	*Hspb1*	*MMP12*	*Oxr1*	*Sirt1*	*Txnl1*
Bcl2	*Cdk2*	*GFAP*	*Htra2*	*Mmp14*	*Park7*	*Sirt2*	*Txnrd1*
Bdnf	*CLEC7A*	*Gnao1*	*Idh1*	*MPEG1*	*Parp1*	*Slc8a1*	*TYROBP*
BLNK	*Cln8*	*Gpr37*	*Il1b*	*Mutyh*	*Pdgfrb*	*Snca*	*Ubc*
Bnip3	*CTSS*	*Gsk3b*	*Il1r1*	*Ncf1*	*Pink1*	*Sod1*	*Ubqln1*
C3	*Cybb*	*Gsr*	*IL2RG*	*Nefh*	*Pla2g4a*	*Sod2*	*Vegfa*
C3AR1	*Cycs*	*Gss*	*Il6*	*Nfe2l2*	*Ppargc1a*	*Sod3*	*Xbp1*

gene. A Benjamini-Hochberg correction using a false discovery rate of 0.2 filtered out random significance due to the many genes tested.

2.11. Neurophysiology recordings and analysis

Animals were placed under isoflurane anesthesia inside of a Faraday cage and connected to a head-stage for high-impedance electrodes (Plexon Inc., Dallas, TX, US). Neurophysiological data was recorded twice per week for 10 min at a sampling rate of 40 kHz (OmniPlex Neural Recording Data Acquisition System, Plexon Inc., Dallas, TX, US) for 9 weeks after implantation. Data was then filtered offline (Offline Sorter, Plexon Inc., Dallas, TX, US) using a high-pass filter followed by a low-pass filter between 300 and 3000 Hz (4-poles, Butterworth filters). Data were digitally referenced to the common average across channels to remove pulse and breathing artifacts, as well as any other common-mode noise. Individual spikes were detected using a -4σ threshold of the root-mean square, automatically sorted using K-means, and manually validated. Calculations of outcome metrics were performed using custom code with MATLAB R2021a (Mathworks, Natick, MA, US) to determine the active electrode yield which was calculated as the proportion of total electrode sites that captured at least one single unit. The spike rate was defined as the inverse of the median interspike interval per unit during every recording session. The peak-to-peak voltage (V_{pp}) was calculated as the sum of the peak and trough values of each ensemble-derived unit waveform. The noise floor was calculated as the root-mean square of the channel after removing spike waveforms. Finally, the signal-to-noise ratio (SNR) of each unit was calculated as the V_{pp} divided by the noise level. Data were binned by averaging the results together into three phases – previously defined by the natural evolution of the foreign body response [62]: acute neuroinflammation between the time of implantation up to 5 weeks, sub-chronic phase between 6 and 11 weeks, and a chronic phase between 12 and 16 weeks. For individual electrode sites that had more than one unit, the Vpp, noise floor and SNR for all detected units were averaged together to yield a single value for each recording session. Based on the 2 mm depth of implantation for the present study, the five most superficial electrode sites lie within the cortical layers L2/3 and L4 (<950 μm depth), the next six electrode sites lie within the cortical layer L5 (<1500 μm depth) and the five most deep electrode sites within cortical layer L6 (<2000 μm depth) [63]. In addition to the bulk analysis of signal quality per electrode site, to further validate this method, we stratified our results into three different cortical depths: superficial, middle, and deep to homogenize the expected response. This stratification method also accounts for micron-scale variability of motor cortex layer between subjects and implantation locations to avoid vasculature. Finally, to further confirm observations, we conducted a comparison recalculating the statistical analysis with each MEA counting as an experimental unit for the phase that showed the largest difference between groups upon single electrode site analysis.

2.12. Electrochemical impedance spectroscopy (EIS) measurements in vivo

Once per week, animals were placed under isoflurane anesthesia inside of a Faraday cage prior to acquisition of electrophysiological recordings to monitor the changes in electrode performance via electrochemical characterization. Electrochemical Impedance Spectroscopy (EIS) was performed with a CH Instruments Electrochemical Analyzer 604E (Bee Cave, TX, US) consisting of each electrode site as the working electrode, and the anchor stainless steel screws on the skull as counter and reference electrodes. EIS was performed over a range of 1–10^5 Hz (12 points per decade) using a 10 mV RMS sinusoidal voltage.

2.13. Statistical analysis

RStudio 2023.06.1 + 524 (RStudio, PBC, Boston, MA, US) was used to curate the compiled data for analysis. GraphPad Prism 10 (Version 10.0.2(232) Dotmatics, Boston, MA, US) and Excel (Microsoft Corporation, Redmon, WA, US) were used to conduct statistical analyses as follows: 1) a Shapiro-Wilk test was done to test for normal distributions, 2) a one-way ANOVA followed by a Tukey post-hoc test was used to compare variables with normal distributions, whereas a Kruskal-Wallis test followed by 3) Benjamini-Krieger-Yekutieli test for multiple comparisons was used for non-normal distributions. The Benjamini-Krieger-Yekutieli test was selected to increase statistical power and reduce type I errors. For immunohistological analysis, a standard Student's *t*-test was used to compare each distance from the implant site within groups. A two-sample z-test of proportions was used to calculate statistical differences in the proportion of active electrodes between groups at each acute, sub-chronic and chronic phase. In all cases, statistical significance was defined as $p < 0.05$ unless otherwise noted. Electrode sites that did not record single units for the entire recording period post-implantation were excluded from the analysis because they may have been defective prior to implantation. Individual wells were considered the experimental unit for the cytotoxicity live/dead assays; tissue from each probe for the immunohistological analysis; and each electrode site for the neurophysiological performance of MEAs (with additional validation calculated with device as the experimental unit, and stratification per cortical layer depth). All results are reported as mean ± standard error of the mean (SEM). Whiskers in boxplots represent the minimum and maximum values, the box represents the first and third quartiles and the horizontal line represents the median. Violin plots represent the distribution of the data.

3. Results

3.1. Effect of sterilized MnTBAP-coated surfaces on cellular viability

In this study, MnTBAP-coated glass coverslips were evaluated with two different cultured cell lines. After 24 h of incubation, we analyzed the proportion of live-to-dead cells to assess the cytotoxicity of the coatings after different sterilization methods. All variables were found to be normally distributed as per the Shapiro-Wilk test ($p > 0.05$) and the one-way ANOVA revealed statistical differences between the positive control and all sterilization methods ($p < 0.0001$), but not within methods. Results in Fig. 1A–B showed that the percentage of dead NIH/3T3 fibroblast cells was similar for MnTBAP-coated surfaces for all sterilization methods (1.61 ± 0.23 %, 1.07 ± 0.18 %, 0.76 ± 0.18 %, and 1.23 ± 0.33 % for ethanol, dry heat, ethylene oxide and autoclave, respectively) and did not differ statistically from the cell viability positive control (0.73 ± 0.12 %; post-hoc Tukey test p-values in Table 2). This indicates that the coating methodology and subsequent sterilization techniques do not cause acute cytotoxicity that could be harmful upon implantation. In contrast, all were statistically significant compared to the cell viability positive control (p-values in Table 1).

As shown in Fig. 1C–D, the effect of sterilized MnTBAP-coated surfaces on microglia/macrophage cell viability was like that which were observed with NIH/3T3 cells. A one-way ANOVA revealed statistical significances between the positive control and all sterilization methods ($p < 0.0001$), but not amongst sterilization methods. Post-hoc testing revealed that the percentage of dead cells was statistically similar (post-hoc Tukey test p-values in Table 2) across all sterilization methods (3.22 ± 0.88 %, 1.59 ± 0.30 %, 1.94 ± 0.67, and 4.10 ± 1.67 % for ethanol, dry heat, ethylene oxide and autoclave, respectively) and the cell viability positive control (4.40 ± 1.14 %). In contrast, all were statistically significant compared to the cell viability positive control (p-values in Table 3). Together these results show that MnTBAP coatings that have undergone sterilization, are not cytotoxic and may be acceptable for *in vivo* evaluation. Ethylene oxide sterilization was implemented as the sterilization technique as it is the preferred method for standard laboratory implantations made with non-coated MEAs.

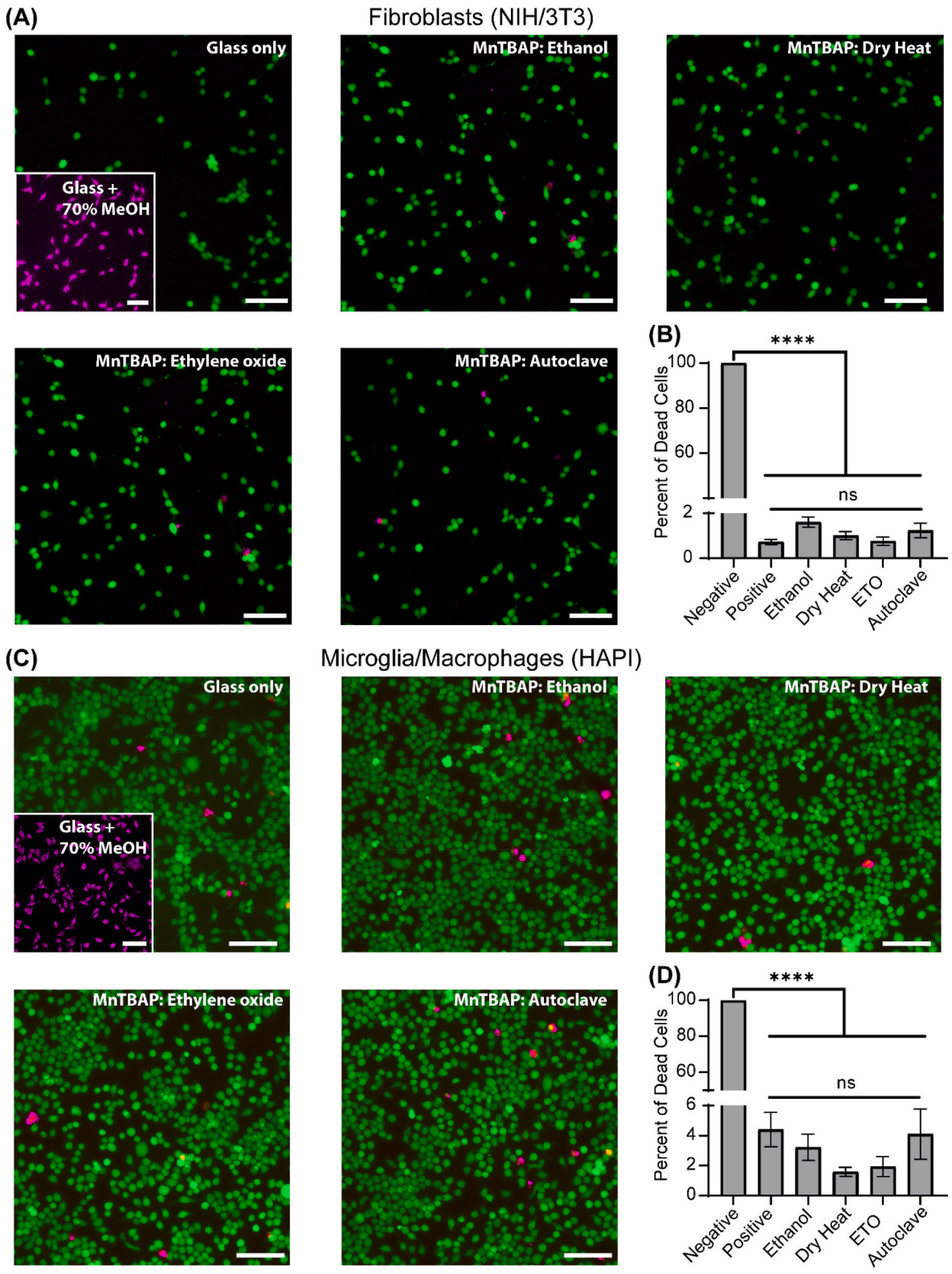

Fig. 1. Cytotoxicity of MnTBAP-coated surfaces sterilized via different methods. Live/dead assay after 24 h incubation on (A) fibroblasts (NIH/3T3) showing cell viability for uncoated positive control (glass only; all live cells), uncoated negative control treated with 70 % MeOH after cell seeding (all dead), MnTBAP-coated and sterilized prior to cell seeding via ethanol, dry heat, ethylene oxide, and autoclave show (B) no significant levels of dead cells for any sterilization method on coated surfaces compared to uncoated controls for NIH/3T3 cells. Same live/dead assay on (C) microglia/macrophage cells (HAPI) after 24-h incubations show similar results (D) for all sterilization methods. Green denotes live cells whereas magenta denotes dead cells. Scale bar = 100 μm. Data reported as Mean ± SEM. Significance levels: ns $p > 0.05$, *$p < 0.05$, **$p < 0.01$, ***$p < 0.001$, ****$p < 0.0001$. N = 18, equally distributed among groups (n = 3 per group). Fluorescent red channel was replaced with magenta to provide a color-blind safe palette. (For interpretation of the references to color in this figure legend, the reader is referred to the Web version of this article.)

Table 2
Tukey test p-values for cytotoxicity of MnTBAP-coated surfaces sterilized via different methods on NIH/3T3 fibroblasts (post-hoc p-values were adjusted for multiple comparisons via the Tukey test method).

	Positive	Negative	Ethanol	Dry Heat	ETO
Ethanol	<0.0001	0.071			
Dry Heat	<0.0001	0.910	0.326		
ETO	<0.0001	0.999	0.086	0.945	
Autoclave	<0.0001	0.497	0.758	0.961	0.564

Table 3
Tukey test p-values for cytotoxicity of MnTBAP-coated surfaces sterilized via different methods on HAPI microglia/macrophages (post-hoc p-values were adjusted for multiple comparisons via the Tukey test method).

	Positive	Negative	Ethanol	Dry Heat	ETO
Ethanol	<0.0001	0.947			
Dry Heat	<0.0001	0.334	0.824		
ETO	<0.0001	0.469	0.925	0.999	
Autoclave	<0.0001	0.999	0.985	0.453	0.604

3.2. Effect of MnTBAP-coated probes on the acute neuroinflammation and neuronal viability

3.2.1. Glial scar formation and blood-brain barrier permeability

Implantation of silicon-based microelectrode arrays can lead to neuroinflammation and recruitment of microglia, macrophages and activated astrocytes around the implant site, leading to encapsulation of the neural interface [64]. Microglia and macrophages facilitate accumulation of reactive oxygen species and other pro-inflammatory molecules, contributing to the failure of the interface [16,19,20,65]. Results in Fig. 2, (all normally distributed; $p > 0.05$), show the neuroinflammatory effect of MnTBAP-coated probes (left) compared to uncoated controls (right). Fig. 2A–B highlights the expression and spatial distribution of reactive astrocytes (Glial Fibrillary Acidic Protein; GFAP) surrounding the implant site (dashed). We found that the use of MnTBAP-coated probes significantly decreased GFAP expression in the immediate region of interest (0–50 μm) from the implant site compared to the uncoated controls ($p = 0.03$), suggesting an improvement on the glial scar formation as early as 2 weeks post-implantation (during the acute phase). As expected, we did not find statistical differences at further distances from the implant site. No significant changes were observed in either macrophage expression (CD68; Fig. 2C–D) nor immunoglobulin G (IgG; Fig. 2E–F) at any distance from the implant site. Together, these results suggest that while accumulation of GFAP expressing astrocytes is diminished with MnTBAP-coated MEAs, there is neither a change to the accumulation of macrophages around the implant site nor the blood-brain barrier permeability.

3.2.2. Neuronal nuclei viability

In addition to glial scar formation and blood-brain barrier permeability, we assessed the neuronal nuclei cell counts around implanted MnTBAP-coated and uncoated control probes. The goal of the MnTBAP coatings is to minimize the accumulation of reactive oxygen species, which should reduce neuronal cell loss. Fig. 2G-H shows the normalized neuron cell count, which was found to be normally distributed (Shapiro-Wilk; $p > 0.05$), at different distances from the implant site. There were no significant differences between MnTBAP-coated and control MEAs at any distance. These results indicate that 2 weeks post-implantation, MnTBAP coatings did not alter neuronal density loss around the implant site. However, there may be differences in NeuN expression for MnTBAP-coated devices at later times post-implantation.

3.3. Electrochemical assessment of MnTBAP-coated MEAs

Our previous electrochemical characterization of MnTBAP-coated and uncoated MEAs revealed no significant differences *in vitro* for the impedance magnitude at 1 kHz for functional devices [41]. Here, we evaluated the *in vivo* electrochemical impedance spectroscopy weekly for all electrode sites and binned the data into the acute (1–5 weeks), sub-chronic (6–11 weeks) and chronic (12–16 weeks) periods. Fig. 3 shows the quantitative analysis of the impedance magnitude (non-normally distributed as per Shapiro-Wilk test; $p < 0.05$) at 1 kHz. Results revealed significant differences ($p < 0.0001$ as per Kruskal-Wallis test) between groups for all three acute, sub-chronic and chronic periods. We found that there were statistically significant differences between the impedance magnitude of MnTBAP-coated and uncoated devices during the acute (1.44 ± 0.06 MΩ for MnTBAP-coated, and 1.69 ± 0.07 MΩ for uncoated; $p = 0.003$), sub-chronic (1.00 ± 0.05 MΩ for MnTBAP-coated and 1.31 ± 0.06 MΩ; $p < 0.0001$) and chronic (0.76 ± 0.03 MΩ for MnTBAP-coated and 1.15 ± 0.06 MΩ; $p < 0.0001$) phases. In addition, both type of arrays showed a significant decrease ($p < 0.001$) from the acute to the sub-chronic and chronic time points. Despite these statistical findings, the change in values for impedance magnitude at 1 kHz do not represent substantial functional differences for the electrode sites because the order of magnitude remains unchanged.

3.4. Effect of MnTBAP-coatings on neurophysiological recording performance of MEAs

Both MnTBAP-coated and uncoated MEAs demonstrated the ability to record spontaneous neural activity from M1 under anesthesia. Exclusions of individual electrode sites from analysis due to not recording any single units for the entire period post-implantation were comparable between groups ($p = 0.59$): a total of 16 electrode sites were excluded from uncoated devices (2.0 ± 0.6 electrode sites per device) were excluded; 14 electrode sites from coated devices (1.6 ± 0.5 electrode sites per device); and 8 from APTES-functionalized devices (1.14 ± 0.5 electrode sites per device). A summary of the total electrode sites excluded per phase can be found in Supplementary Table S1. Fig. 4 shows representative neurophysiological recordings from MnTBAP-coated and uncoated MEAs during three sessions at different post-implantation time-periods. From these representative traces, it is apparent that coating MEAs with MnTBAP results in a higher number of units per electrode and a higher spike rate. Quantitative analyses shown in Figs. 5 and 6 confirmed these observations (all variables were non-normally distributed as per Shapiro-Wilk test).

In Fig. 5, the proportion of active electrodes was found to be comparable (two-sample z-test of proportions) between groups upon implantation (MnTBAP: 46.6 % vs. Uncoated: 55.0 %; $p = 0.89$) and observed a quick increase by week 2 (MnTBAP: 67.7 % vs. Uncoated: 80.4 %), where uncoated devices had a significantly higher proportion ($p = 0.01$); however this trend reversed and for almost every week between weeks 7 and 14 MnTBAP-coated devices (ranging between 60.0 % and 74.6 %) had a significantly ($p < 0.05$) higher proportion of active electrodes compared to uncoated controls (ranging from 50.9 % to 58 %). The last two weeks of recordings showed a convergence of the proportion of active electrodes between groups (MnTBAP-coated: 60 % and Uncoated: 66 % by the end of the 16 weeks; $p = 0.83$). We recorded week 17 from a subset of animals (MnTBAP-coated: $n = 4$, Uncoated: $n = 4$) and found a transient increase for coated devices (75 %) but not for uncoated devices (63 %). We did not conduct statistical analysis on this week due to the small sample size. From the weekly analysis of these results, we observed week-to-week variations, perhaps biological in nature or due to subtle differences in animal handling or timing during the day of recording sessions. Because of this, we decided to bin the data (Fig. 5B) into three phases: acute (1–5 weeks), sub-chronic (6–11 weeks) and chronic (12–16 weeks), which are consistent with described temporal changes following implantation of intracortical microelectrode

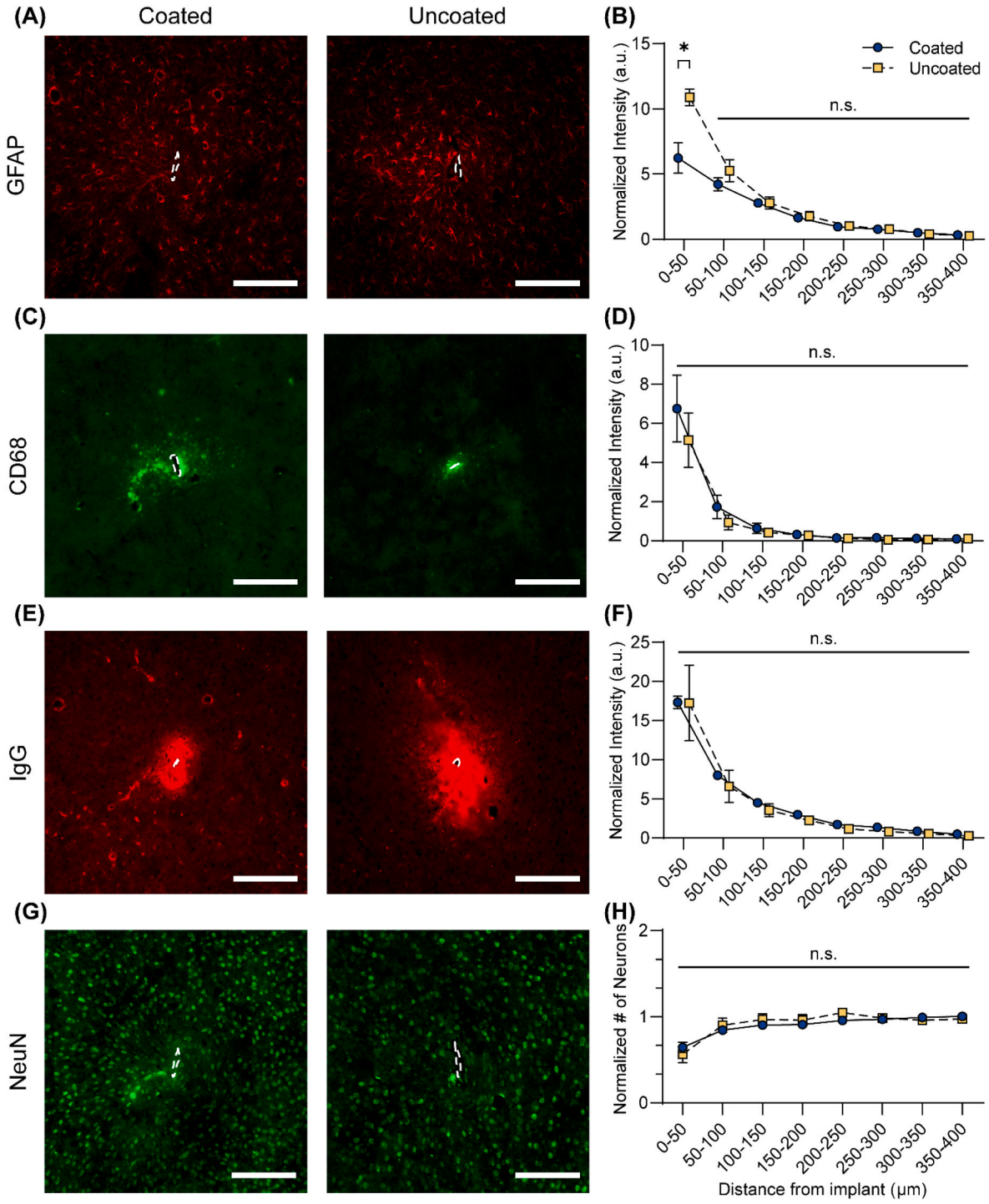

Fig. 2. Effect of MnTBAP-coatings on tissue two weeks after intracortical MEA implantation. Representative images of immunohistology and distribution profiles from the center of the implant site (white dashed line) for (A–B) astrocytes (GFAP) showed significant differences between Coated (left) and uncoated (right) controls only within 50 μm. In contrast, (C–D) activated microglia and macrophages (CD68), (E–F) blood-brain barrier breach (IgG), and (G–H) neuronal nuclei (NeuN) showed no significant differences at two weeks. Scale bar = 200 μm. Data reported as Mean ± SEM. Significance levels: ns $p > 0.05$, *$p < 0.05$, **$p < 0.01$, ***$p < 0.001$, ****$p < 0.0001$. N = 3.

arrays [66–68]. We included the analysis of APTES-functionalized devices to further assess the possibility that the intermediate treatment steps performed to coat devices (e.g., cleaning and APTES coating) may contribute to any effect observed between groups. Results confirmed the previous results, where the proportion of active electrodes was comparable for all groups during the acute phase (Uncoated: 70 %, MnTBAP: 66.9 %, and APTES: 71.2 %; $p > 0.05$). The uncoated controls showed a decline between the acute and sub-chronic (50 %; $p = 0.001$), and chronic (58 %; $p = 0.03$) periods but no change between sub-chronic and chronic ($p = 0.88$). The MnTBAP remained largely stable between all three phases with no significant changes ($p > 0.05$). In contrast, the APTES-functionalized devices experienced a decline between the acute to sub-chronic (54 %; $p = 0.002$), and between the sub-chronic to chronic (26 %; $p < 0.0001$) phases. Interestingly, the most catastrophic decline for this group was observed between the sub-chronic and chronic phases ($p < 0.0001$). These results suggest that MnTBAP is

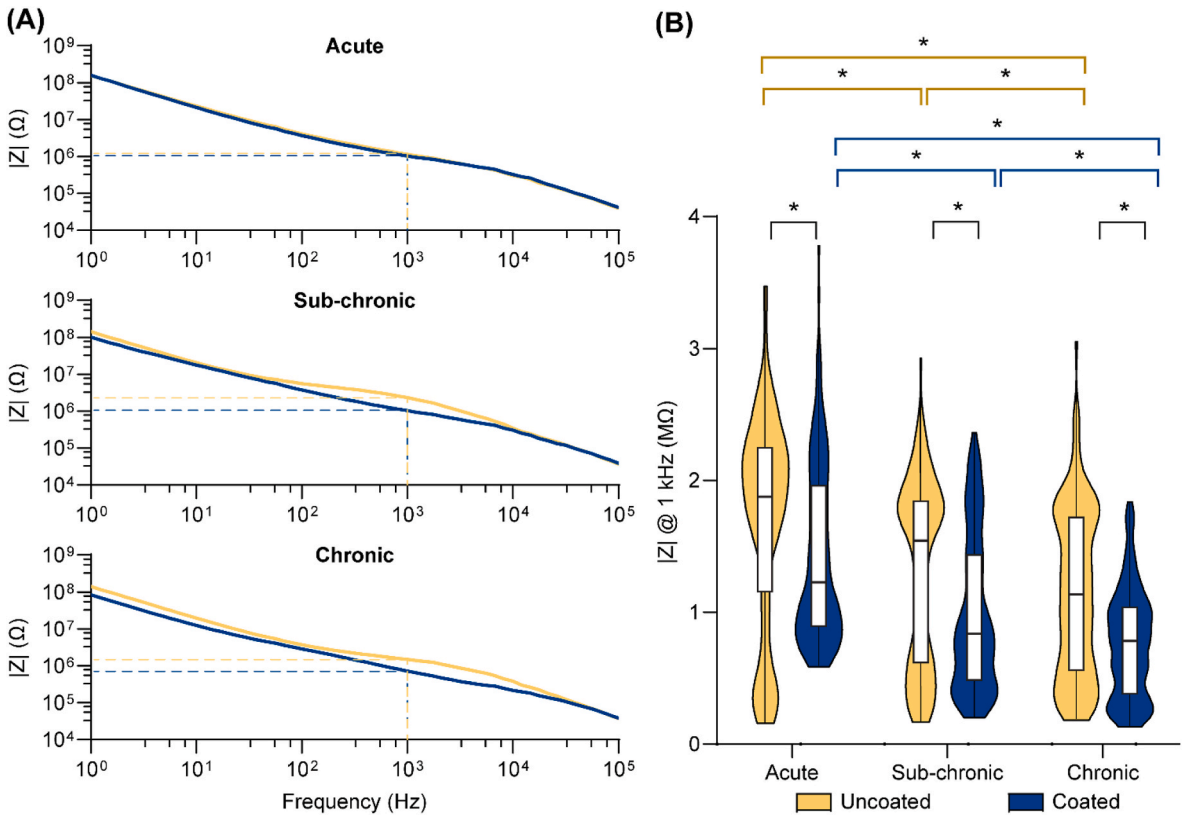

Fig. 3. *In vivo* electrochemical impedance spectroscopy. Representative traces for a single electrode site during the (A) acute (top) sub-chronic (middle), and chronic (bottom) period post-implantation. (C) Violin and boxplots of the impedance magnitude at a frequency of 1 kHz. Horizontal line of the boxplot represents the median and the whiskers represent the maximum and minimum points; width of the violin plots represents data distribution. Significance levels: *p < 0.05.

capable of stabilizing the proportion of active electrodes over chronic implantation periods, and the effects are not a result of functionalization of electrode surfaces by APTES. As a secondary validation of our methodology, we conducted a comparison recalculating the statistical analysis with each MEA counting as an n = 1 for the sub-chronic phase. The sub-chronic phase was selected due to this phase demonstrating the largest difference between groups upon single electrode site analysis. Results confirmed our previous observations, where the difference between uncoated and MnTBAP groups was statistically significant (p = 0.02).

Because of glial scarring, neuronal density and neurophysiological recordings may not be homogeneous along the cortex but rather layer-specific, we furthered our analysis by stratifying our results into three different cortical depths: superficial (L2/3 & L4), middle (L5), and deep (L6) to homogenize the expected response, as shown in Fig. 5C. A weekly breakdown of these results can be found in Supplementary Fig. 1. Unsurprisingly, results showed that there was a lower proportion of active electrodes in the deeper electrode sites, presumably due to lower neuronal density. However, improvement of proportion of active electrodes as a result of using MnTBAP-coated devices was consistent regardless of the depth of implantation; MnTBAP-coated devices showed consistent proportion of active electrodes throughout the study, while the uncoated devices showed a decline, especially between acute and sub-chronic phases post-implantation. Finally, the average number of units detected per electrode site was consistent with the observations described for the proportion of active electrodes, suggesting that the number of active neurons around the implant site is preserved in MnTBAP-coated MEAs compared to uncoated controls over the implantation period and further supports the use of MnTBAP coatings on MEAs.

Analysis of neurophysiological recording (all variables were non-normally distributed) quality revealed a similar median spike rate (Fig. 6A) as per the Kruskal-Wallis test followed by the Benjamini, Krieger and Yekutieli post-hoc test between groups during the acute (Uncoated: 6.57 ± 0.45 1/s, MnTBAP-coated: 6.88 ± 0.53 1/s; p > 0.05) and chronic (Uncoated: 5.99 ± 0.58 1/s, MnTBAP-coated: 6.76 ± 0.62 1/s; p > 0.05) phases, but statistically different during the sub-chronic phase (Uncoated: 4.79 ± 0.39 1/s, MnTBAP-coated: 6.88 ± 0.54 1/s; p = 0.04). In addition, the uncoated controls experienced a significant decrease between the acute and sub-chronic phases (p = 0.04), whereas the rate remained constant for the MnTBAP-coated units (p > 0.05), suggesting a stable median spike rate after implantation. As shown in Fig. 6B, the V_{pp} of active channels (i.e., excluding channels that did not detect single units for at least 50 % of the weeks in the phase bin; see Supplementary Table 1 for sample sizes) significantly decreased post-implantation for both groups (p < 0.05), suggesting that the MnTBAP was not protective against loss of signal amplitude. The RMS noise floor of active electrodes shown in Fig. 6C (p < 0.001 as per Kruskal-Wallis) was statistically lower for MnTBAP-coated for all three phases (acute: 7.55 ± 0.19 μV, sub-chronic: 6.24 ± 0.22 μV, and chronic: 6.02 ± 2.19 μV) compared to uncoated devices (acute: 8.84 ± 0.18 μV, sub-chronic: 7.48 ± 0.26 μV, and chronic: 6.69 ± 0.22 μV; p < 0.0001, p < 0.0001, and p = 0.005, respectively); however, both groups experienced a decrease throughout the study. Due to the comparable V_{pp} and significant differences in the noise floor, the changes in SNR (Fig. 6D) were found to be statistically significant for all three phases between MnTBAP-coated (acute: 11.21 ± 0.38, sub-chronic: 10.88 ± 0.35, and chronic: 10.30 ± 0.34) and uncoated devices (acute: 9.73 ± 0.21, sub-chronic: 8.83 ± 0.19, and chronic: 8.83 ± 0.17; p = 0.03, p < 0.0001, and p = 0.001, respectively). In addition, The SNR decreased for the uncoated devices between the acute and sub-chronic (p = 0.004), and chronic (p = 0.005) phases but not between sub-chronic and chronic (p > 0.05). In contrast, the SNR of MnTBAP-coated devices remained stable between all three phases (p > 0.05). Altogether these results suggest that

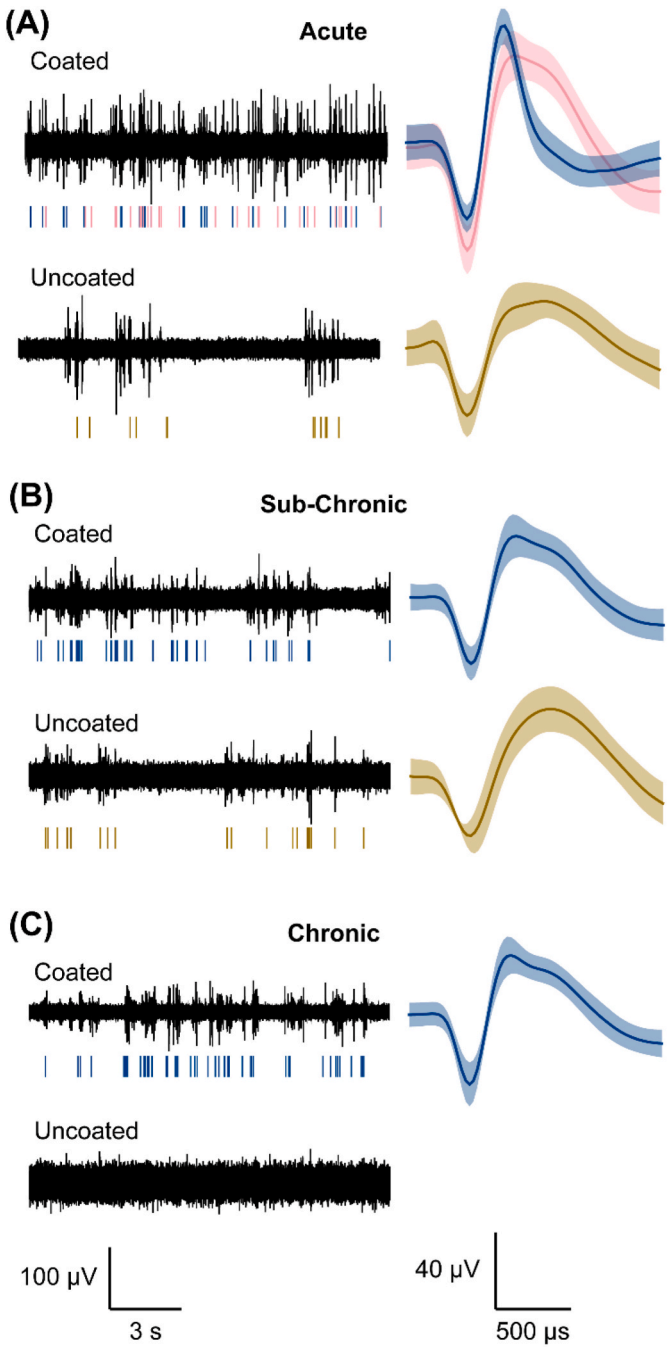

Fig. 4. Neurophysiological recordings of coated and uncoated probes during the acute (1–5 weeks), sub-chronic (6–11 weeks), and chronic post-implantation periods (12–16 weeks). Representative recordings and single units single channels during the acute (A) sub-chronic (B) and (C) chronic periods for coated (top) and uncoated (bottom) MEAs showing raster plots (under recording) and average single units detected (right).

the MnTBAP coating on intracortical MEAs have a positive effect on the recording quality and performance of electrode sites that demonstrate a stable signal quality over chronic implantations.

3.5. Effect of MnTBAP-coated probes on the chronic neuroinflammation and neuronal viability

3.5.1. Assessment of neuroinflammatory gene expression

To understand the neuroinflammatory and oxidative stress response in the brain, we performed experiments with a third cohort of animals that received non-functional implants of each type: uncoated control, APTES-coated, and coated (MnTBAP-coated). In this third cohort, animals survived for 2-, 7-, or 11- weeks post-implantation. We performed pair-wise comparisons between treatment groups to understand relative differential gene expression levels between the groups. Rather than using histological markers, as we initially did for the first cohort, we developed a custom gene expression panel with 152 genes associated with neuroinflammatory and oxidative stress pathways (Table 1). Here, our results from bulk gene analysis based on log2(fold change) of uncoated control vs. APTES, uncoated control vs. MnTBAP-coated, and APTES vs. MnTBAP-coated for each of the three defined time points. Comparisons that did not demonstrate significant levels of differential gene expression between the groups were not presented here. Only three comparisons demonstrated significant differences in differential gene expression for the gene sets that we examined (Fig. 7).

Fig. 7A shows that two genes were differentially expressed between APTES-coated and MnTBAP-coated implant groups at 2 weeks post-implantation. Specifically, Prostaglandin-Endoperoxide Synthase 2 (*Ptgs2*) was significantly upregulated in the MnTBAP-coated group compared to the APTES-coated at 2 weeks post-implantation. *Ptgs2* is a protein encoding gene, responsible for regulating the expression levels of antioxidative enzymes [69]. Thus, increased Ptgs2 expression would suggest increased antioxidative enzyme production for MnTBAP-coated devices compared to the APTES-coated devices. Additionally, in the same comparison, Solute Carrier Family 8 Member 1 (*Slc8a1*) was differentially upregulated in the APTES-coated group compared to the coated group at 2 weeks post-implantation. *Slc8a1* has been shown to be required for amplifying inflammatory and antimicrobial MΦ responses [70]. Taken together, the gene expression results confirm the above histological results in suggesting that the APTES-coated group is more inflammatory activated than the MnTBAP-coated group at 2 weeks post-implantation.

At 11 weeks post-implantation, we found two genes to be significantly differentially expressed in the uncoated control vs. MnTBAP-coated implants comparison. Both Sirtuin 2 (*Sirt2)* and Glutathione S-Transferase Pi 1 (*Gstp1)* were differentially increased in expression levels in the uncoated control group compared to the MnTBAP-coated group (Fig. 7B). *Gstp1* has been reported to prevent sepsis-related inflammation [71] and it has also been shown that increased *Gstp1* expression is a cellular responses to oxidative stress or proinflammatory stimuli [72]. *Sirt2* has been shown to inhibit the transcription of pro-inflammatory genes [73], and inhibit growth cone collapse and neurite outgrowth [74,75]. Therefore, the neuroinflammatory gene expression profile for MnTBAP-coated devices is more favorable than that associated with uncoated control devices.

3.5.2. Qualitative assessment of traditional neuroinflammatory markers

To complement the robust evaluation of neuroinflammatory gene expression performed on 2-, 7-, and 11-weeks post-implantation samples, representative animals of the second cohort were selected for more traditional immunohistochemical staining to assess the 16-week time point. Tissue from one animal implanted with an uncoated control MEA and one animal implanted with a MnTBAP-coated MEA was stained for common markers of neurons (NeuN), blood-brain barrier damage (immunoglobin G infiltration, IgG), microglia activation (cluster of differentiation 68, CD68), and astrocytic scaring (glial fibrillar acid protein, GFAP). Stained tissue was imaged on a confocal microscope and is displayed here for qualitative assessment only (Supplementary Fig. 4).

Neuronal density was assessed with NeuN suggests that neurons were equally as close to the implant surface in both uncoated controls and MnTBAP-coated implants. There also appears to be more NeuN positive cells in the surrounding 50 µm radius of the uncoated control implants than the MnTBAP-coated implants. In the animals that we examined; blood-brain barrier permeability (IgG expression) appears to be more pronounced in the coated animal compared to uncoated control animal. Likewise, microglia/macrophage activation (CD68 expression)

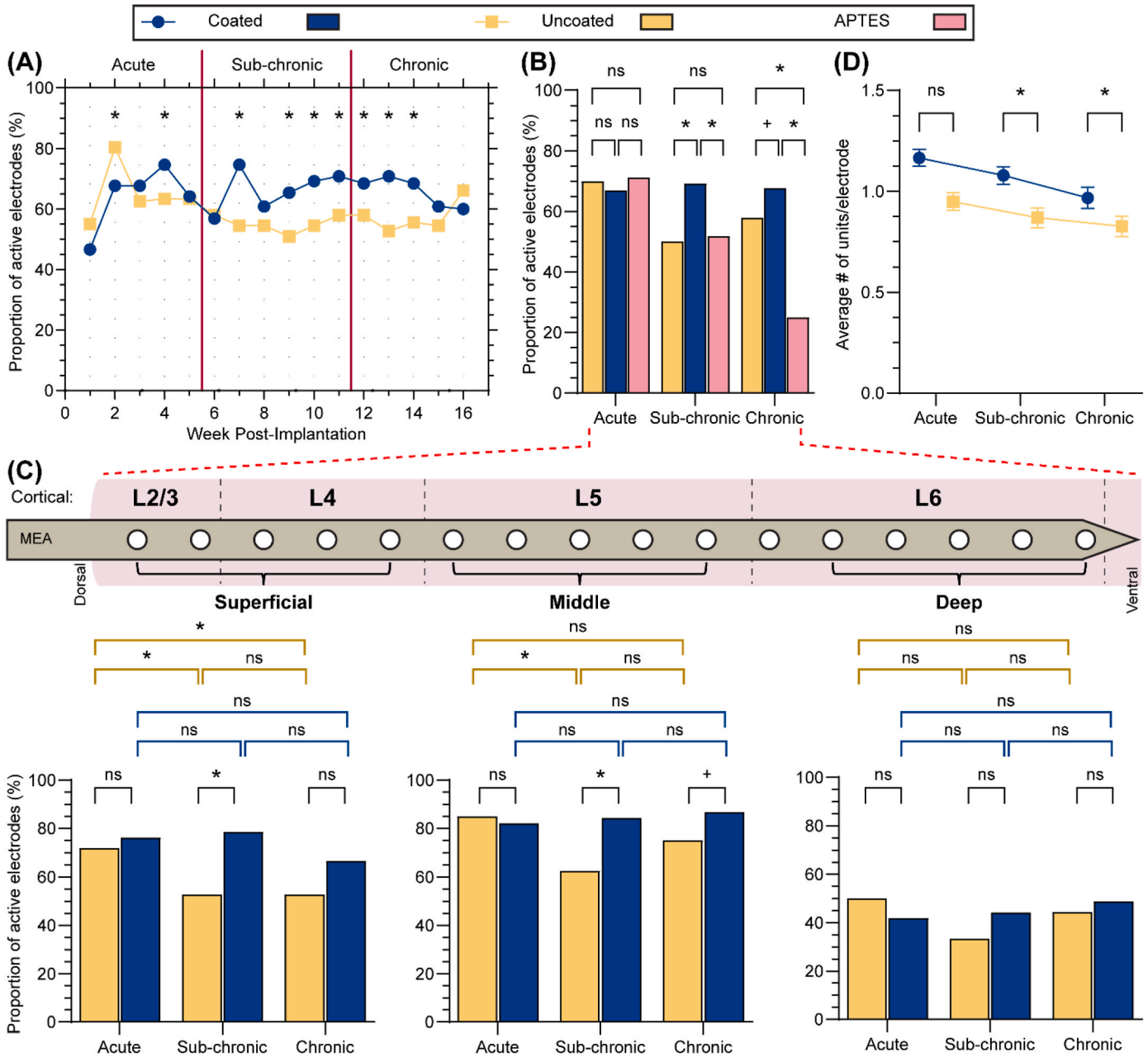

Fig. 5. Quantification of coated and uncoated intracortical MEAs performance. (A) Weekly proportion of active electrodes in uncoated and coated devices 16 weeks post-implantation and (B) binned to summarize findings as they relate to progression of the neuroinflammatory process as acute (1–5 weeks), sub-chronic (6–11 weeks), and chronic (12–16 weeks) periods post-implantation. Inset (C) is the analysis of proportion of active electrodes with grouping by cortical depth; superficial (left) electrode sites are targeting layers 2/3 and 4; middle (middle) electrode sites are targeting mostly layer 5; and deep (right) electrode sites are targeting mostly layer 6. (D) Number of single units detected per electrode site binned into acute, sub-chronic and chronic periods post-implantation. Significance levels are as following ns $p > 0.10$, + $p < 0.10$; *$p < 0.05$.

shows a lower presence in the control uncoated animal with higher levels around the implant site in the MnTBAP-coated implant animal. However, astrocytic scarring (GFAP expression) indicates higher gliosis immediately around the implant in the uncoated control implanted animal, whereas the MnTBAP-coated implanted animal demonstrated a lesser response at the implant site. Taken together, these results suggest that the MnTBAP coating is able to reduce the astrocyte contribution to the glial scar around the implant, and still maintain neurons close to the implant site, which contributes to our understanding of the noted improvements observed on the neural recording signal quality.

4. Discussion

Implantation of MEAs initiates a neuroinflammatory cascade and produces reactive oxygen species, which may contribute to the failure of neural interfaces. However, this phenomenon is likely a multifactorial consequence [76]. Recent evidence [19,29–31] has demonstrated that the use of natural antioxidants can modulate the neuroinflammatory cascade by reducing the accumulation of reactive oxygen species. In the current study, we have demonstrated that coating MEAs with MnTBAP can provide stable recording quality over chronic (up to 16 weeks) periods of implantation while reducing glial scar formation around the implant site as soon as 2 weeks post-implantation and reduced the

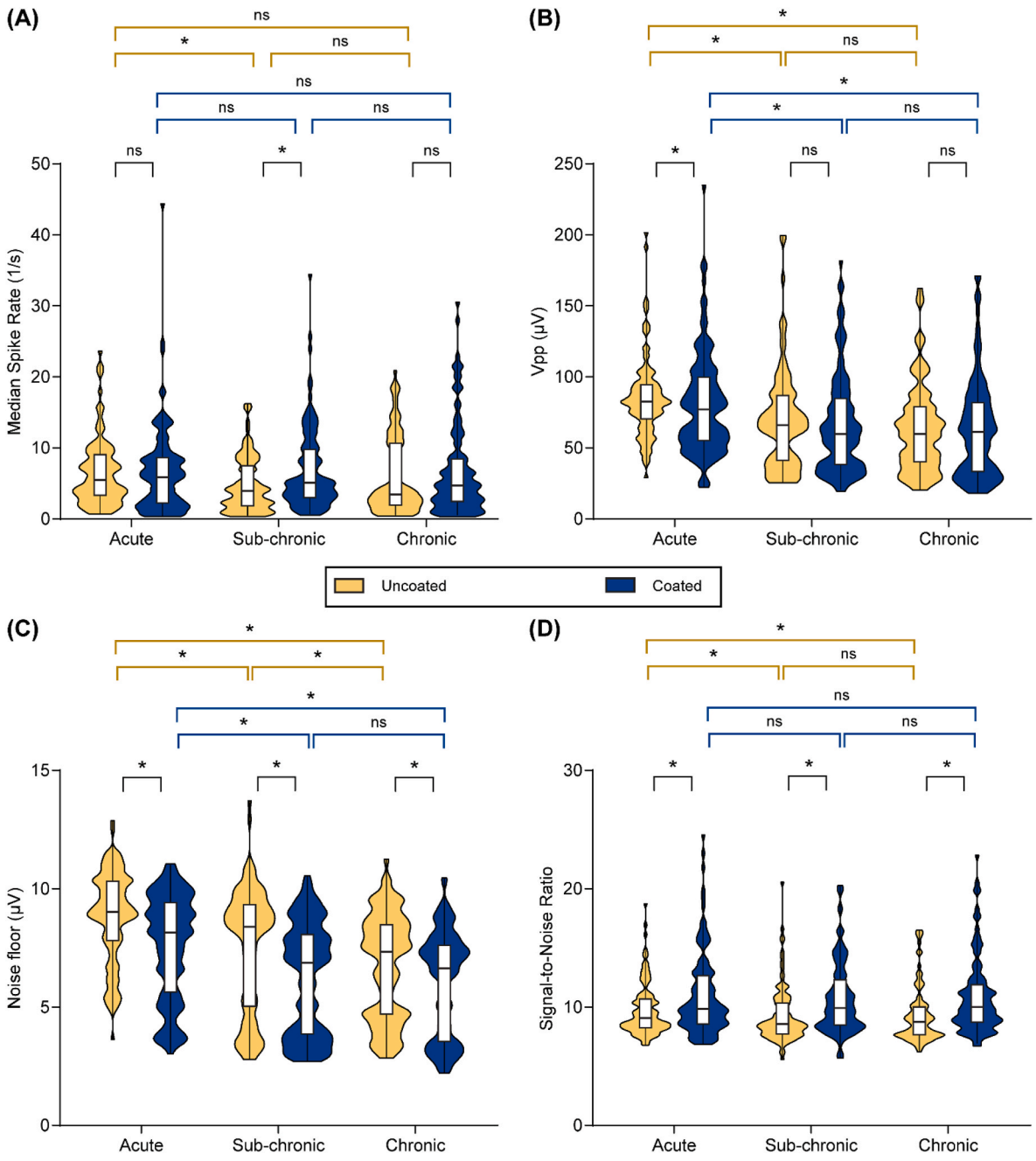

Fig. 6. Quantification of coated and uncoated intracortical MEAs recording quality. (A) median neuronal spike rate, (B) voltage peak-to-peak, (C) RMS noise floor, and (D) signal-to-noise ratio. Horizontal line of the boxplot represents the median and the whiskers represent the maximum and minimum points; width of the violin plots represents data distribution. Significance levels: ns $p \geq 0.05$, *$p < 0.05$. Statistical comparisons with blue lines represent comparisons between phases for the coated devices; yellow lines represent comparisons for the uncoated devices. See electrode site sample size per period in Supplementary Table A. (For interpretation of the references to color in this figure legend, the reader is referred to the Web version of this article.)

differential expression of neuroinflammatory genes at 11 weeks post-implantation, in the middle of the stretch of time with consistently improved recording performance for MnTBAP-coated devices. In contrast, uncoated control devices experienced a loss signal quality over time, consistent with results throughout the field.

4.1. The effect of MnTBAP coatings on astrocytes, macrophages, microglia, and neurons

The 2-week histology here showed lower levels of reactive astrocytes as measured through GFAP expression (Fig. 2A–B) for MnTBAP-coated implants compared with uncoated control implants. Qualitative analysis of 16-week histology continued to show lower levels of reactive astrocytes around the implant site (Supplementary Fig. 4). This is important because, upon implantation of MEAs, macrophages and microglia respond to the localized injury and presence of a foreign body changing from an anti-inflammatory to a pro-inflammatory state [77–79]. Inflammatory microglia facilitate the recruitment of astrocytes to the implant site within a few hours [80]. Glial cells in the reactive state increase expression of reactive oxygen species, cytokines, other pro-inflammatory mediators, and neurotoxic factors. Reactive glial cells, which act as intercellular messengers under normal circumstances [81], are not capable of carrying their normal functions, further altering the microenvironment by exacerbating expression of reactive oxygen

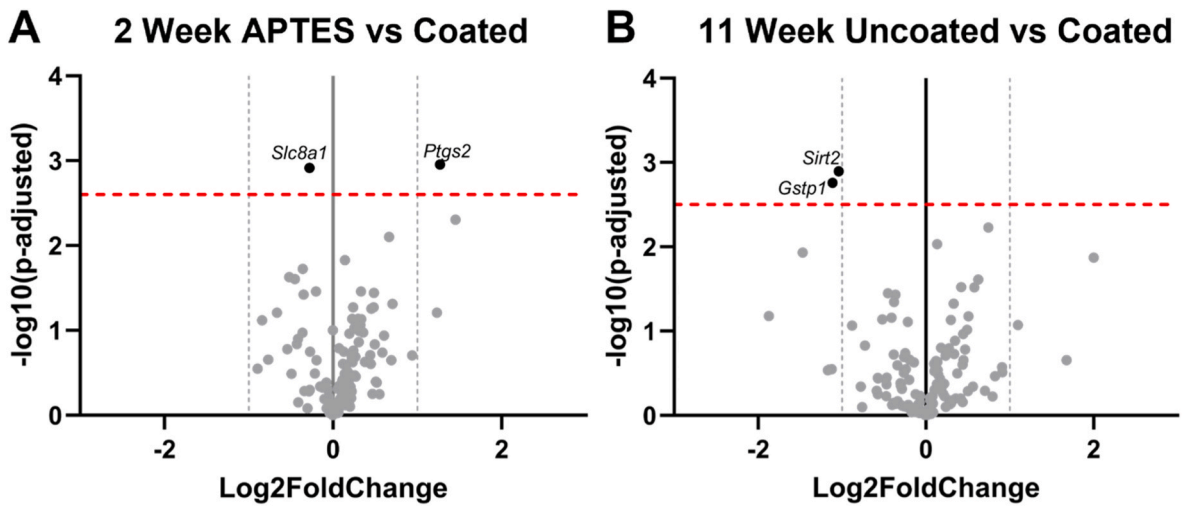

Fig. 7. Bulk gene analysis tissue isolated adjacent the implant site. Custom gene panels examined the differential expression of 152 oxidative stress and neuroinflammatory genes associated with neural implants. Log2(fold change) is based on differential expression between pairs of uncoated control vs. APTES-coated, uncoated control vs. MnTBAP-coated, or APTES-coated vs. MnTBAP-coated at 2-, 7-, or 11 weeks post-implantation with a 2-tailed unequal variance *t*-test for each gene. Combinations not visualized in this figure did not present with any significantly differentially expressed genes. Comparisons with significant differential gene expression included: (A) APTES vs MnTBAP-coated at 2 weeks and (B) Uncoated control vs. MnTBAP-coated at 11 weeks. Grey points indicate genes with no significant difference in the comparison, Black points (above the red dashed line) were significant. N = 9 with n = 3 for each group. (For interpretation of the references to color in this figure legend, the reader is referred to the Web version of this article.)

species, and resulting in homeostasis loss [80,82]. Such loss of homeostasis in the microenvironment results in negative effects on the excitability of neurons around the implant site, which could result in a decrease in spiking rate of neighbouring neurons [80,83–86]. In addition, it has been shown that formation of the glial scar is associated with changes in electrochemical impedance and worsening of the quality of the recorded signals [80,87–91]. These effects contribute in part to failure of the interface, resulting in loss of the signal quality over time and neuronal loss. The stability of the signal quality and neuronal activity preservation in MnTBAP-coated devices – as shown by the unchanged proportion of active electrodes, spike rate, and SNR between phases (Figs. 5 and 6) – could potentially be attributed to mitigation of the glial scar formation around the implant site that reduce the accumulation of reactive oxygen species local to the implant-tissue interface. Of importance, we did not assess the oligodendrocyte (e.g., myelination) expression near implanted electrodes, which has been related to MEA loss of performance [23,92]. However, the neuroinflammatory gene expression panel does include several genes that are associated with neuronal viability.

Microglia and macrophages have been identified as closer to the surface of the MnTBAP-coated implants than astrocytes. However, microglia have been shown to be the source of ROS, and could be expected to be less “impacted” by the presence of an ROS scavenger [93]. Astrocytes and neurons generate less ROS and have more defences against ROS. Astrocytes even release antioxidants [94]. Therefore, it is plausible that astrocytes are more effected than microglia by the MnTBAP coatings.

While NeuN has been successfully used for over 20 years as a marker for postmitotic neurons [95], concerns still exist about the variety of reasons that could impact NeuN expression levels. Additionally, GFAP + astrocytes have also been shown to express NeuN [95]. Therefore, IHC alone should be interpreted with caution and more robust analysis should be included, such as gene expression or whole transcriptome analysis. Considering the field moving in this direction [58,59,96–98], we have complemented our IHC with additional markers for neuron viability utilizing a custom gene array panel, Table 1.

4.2. The effect of MnTBAP coatings on the blood-brain barrier

Another concern during implantation of intracortical MEAs has been interference of normal oxygenation resulting from vascular damage that mimics localized ischemic (in the case of vascular occlusion from thermal damage from drilling or cortical dimpling during insertion [99,100]) or haemorrhagic stroke (in case of artery or vein rupture during insertion) both of which can disrupt the blood-brain barrier [19,101]. Disruption of normal oxygenation can exacerbate accumulation of reactive oxygen species because by-products originating from the breakdown of blood infiltrate brain tissue from the disrupted blood-brain barrier [11,99,102–105]. Interestingly, blood-brain barrier permeability resulting from such disruption can not only be seen during the acute phase, but also during the sub-chronic and chronic phases [14,102]. Such permeability changes the composition of the immediate microenvironment [102], which can lead to adsorption of these reactive oxygen species and inflammatory molecules to the materials of the arrays (e.g., metals, silicon, polymers which are relatively hydrophobic [106–109]), perpetuating the neuroinflammatory cascade resulting in subsequent breakdown of the blood-brain barrier, neurodegeneration, and demyelination [11,12,49]. Such events are further evidenced by previous investigations [16,64] which have uncovered that astrocytic expression around stab wounds of the same dimensions as MEAs (e.g., intracortical implantation of MEA immediately followed by device removal) resolve within 4 weeks post-injury, but not in sub-chronic implants (e.g., implant not removed after insertion). Here, we found infiltration of IgG after implantation of MnTBAP-coated devices, indicating that MnTBAP coatings cannot mitigate the disruption of the blood-brain barrier. It was not unexpected that blood-brain barrier permeability resulting from the trauma of implantation was unaffected at an acute timepoint post-implantation as the coating is not designed to protect against blunt and sharp trauma.

4.3. Implications of MnTBAP coatings on the fate of the neuronal recordings

The persistent neuroinflammatory response associated with intracortical MEA implantation has been documented to reduce neuronal cell viability, correlated with in a lower proportion of active electrodes, and

changes to the neurofilament of projecting axons [11,23,64,83,92,110]. Both changes start in the immediate regions to the implant sites ranging from 0 μm up to 230 μm [64,102]. The proximity of the neuronal density to the MEA surface is important because recording from individual neurons has been experimentally determined to extend up to 140 μm from the electrode site [24,25]. As seen in Fig. 4, we observed no significant differences in NeuN density between MnTBAP-coated and uncoated probes despite evidence that neuronal death can occur during the acute phase post-implantation [64,102]. The results of the present study on the proportion of active electrodes and the number of units support the notion that MnTBAP coatings have preserved neuronal function. This is evidenced by the unchanging proportion of active electrodes between phases for MnTBAP-coated devices and an observed 11 % decrease in average number of units per electrode site between the acute and chronic phases for MnTBAP-coated devices compared to 21 % decrease for uncoated control devices. Furthermore, spike rate is relevant to MEA performance because the implantation of MEAs can affect not only neuronal viability but also neuronal function [102]. Here, we demonstrated that the spike rate for MnTBAP-coated devices was statistically unchanged throughout the implantation period, whilst uncoated devices experienced a decrease in firing rate, especially between the acute and sub-chronic phases. Similarly, the SNR was stable for MnTBAP-coated devices but declined over time for uncoated devices, especially between acute and sub-chronic phases, suggesting that signal quality can be preserved by using MnTBAP coatings. Finally, it is important to note that loss of NeuN positive cell staining can also be a result of temporary suspension in synthesis due to damage, and not necessarily loss [111,112]. Therefore, employing transcriptomics to investigate a complete set of genes associated with neuron viability [113] as well as investigation of more the chronic response to MnTBAP-coated MEAs will be critical to establishing a robust understanding of the impact and mechanisms associated with improved recordings on MnTBAP-coated MEAs.

4.4. The effect of reactive oxygen species on MEAs

Reactive oxygen species are not only damaging to tissues, but also to the materials of the MEAs. In the study by Takmakov et al. [20] different styles of commercially-available MEAs were systemically exposed to reactive oxygen species at higher than physiologically-occurring concentrations (10–20 mM compared to 0.1 μM in homeostasis) of reactive oxygen species in an accelerated aging study to simulate oxidative stress (which is estimated to occur at concentrations of 1 mM [114]). The group found delamination of insulation materials (e.g., Parylene-C, silicon oxide, etc.), causing electrochemical changes associated with an increase in the exposed surface area of the metal, resulting in a decrease of the impedance. Kozai et al. [115], Takmakov et al. [20], Black et al. [116] and Barrese et al. [117] among others, have also found cracks in the insulation materials which further influence the electrochemical changes to the MEAs, leading to loss of long-term electrode recording functionality. Electrochemical impedance profiles shown in Fig. 3 suggest that there were changes between the acute, sub-chronic and chronic phases; however, the MnTBAP coating did not seem detrimental to electrode performance, possibly because the magnitude of the changes was not expected to have a functional effect. Furthermore, here, we did not evaluate the direct effect of the coatings on the accumulation of reactive oxygen species; however, our previous studies [16,31,35,51] have demonstrated a reduction of multiple superoxide anions *in vitro* and expect these results to be translatable to the *in vivo* environment. Quantitative gene expression identified that uncoated control implants differentially expressed higher levels of *Gstp1* and *Sirt2* compared to MnTBAP-coated devices. *Sirt2* has been shown to inhibit the transcription of pro-inflammatory genes [73], and inhibit growth cone collapse and neurite outgrowth [74,75]. Either of these two possible consequences of higher *Sirt2* expression could contribute to our understanding of the role of neuroinflammation in decreased microelectrode recording performance. Similarly, increased *Gstp1* expression has been associated with cellular responses to oxidative stress or proinflammatory stimuli [72], suggesting that a source of the decreased neuroinflammatory response to MnTBAP-coated devices could be linked to oxidative stress.

4.5. Other interventions to improve electrode performance

Other investigators have attempted to improve the recording reliability of intracortical MEAs for neuroprosthetic applications. Most closely related to the current study, Zheng et al. [118] built upon our preliminary work with MnTBAP coatings [35] to modulate the accumulation of reactive oxygen species using manganese(III) meso-tetrakis-(N-(2-aminoethyl)pyridinium-2-yl) porphyrin, with successful preservation of cell viability. Unfortunately, Zheng et al. did not report a sustained histological effect beyond one-week post-implantation, or report on the impact on MEA recording performance. Previous research by our group examined different interventions to improve mid- and long-term recordings from intracortical MEAs including the use of the naturally-derived products resveratrol and curcumin. Resveratrol was systemically delivered before or daily after implantation, resulting in short- [29,119] and long-term [19] decrease of reactive oxygen species, and improvements to neuronal cell density and improvement of blood-brain barrier instability in spite of mild injury to liver when administered repeatedly via intraperitoneal route. We have explored other efforts to develop resveratrol-release devices that have also low moduli [51,119]. Results suggest that release is short-lived and the effects of resveratrol quickly disappear. However, the soft, low modulus of flexible devices appears to provide an added benefit to neuronal cell preservation. A different delivery mode for resveratrol that we have investigated is ventricular (brain) delivery [50]. However, results indicate that this approach may not be ideal as suggested by an increase of other neuroinflammatory markers.

Building from prior work [35,41] we have demonstrated the use of this novel superoxide scavenger, MnTBAP, as a MEA coating that can minimize glial scar formation (Fig. 2A–B), increase the proportion of active electrodes (Fig. 5A–B), spike rate (Fig. 6A), and overall signal quality by increasing SNR (Fig. 6D). Our results here suggest that the modified surfaces provided anti-oxidative activity over the course of 16 weeks post-implantation, as reflected by the improved recording performance. Additionally, *in vitro* studies with BV-2 microglial cells indicated a significant reduction of intracellular and extracellular reactive oxygen species when cultured on composite MnTBAP surfaces [35]. A major advantage of the MnTBAP coating used here is that it is self-contained without the need for systemic injection of pharmacological substances. While the degree of degradation of the MnTBAP coating that may result from implantation is unknown, the coating appears to improve recording reliability and future studies will address the impact of the coating under chronic implantation conditions.

5. Conclusions

The data presented here demonstrate that the MnTBAP coatings are non-cytotoxic in neural tissue and that they acutely reduce glial scar formation around an implant site, while chronically reducing the expression of neuroinflammatory and neurodegenerative genes, coinciding with improvements in improved neural recording quality in the acute (1–5 weeks), sub-chronic (6–11 weeks) and chronic (12–16 weeks) neuroinflammatory phases. We concluded that these positive effects were a direct result of the MnTBAP coating, as this synthetic molecule is available, and we are not aware of mechanisms for biological or hydrolytic degradation. Future studies will assess the integration with other strategies that reduce the foreign body response such as reduction of the cross-sectional area and stiffness of the implant.

Disclosures

The contents do not represent the views of the U.S. Department of Veterans Affairs, the National Institutes of Health, or the United States Government. Any opinion, findings, and conclusions or recommendations expressed in this material are those of the authors(s) and do not necessarily reflect the views of the National Science Foundation.

Institutional review board statement

All animal care, handling and procedures were performed in compliance ARRIVE guidelines and National Research Council's Guide for the Care and Use of Laboratory Animals. Protocols were approved by the Institutional Animal Care and Use Committees (IACUC) at Louis Stokes Cleveland Department of Veterans Affairs Medical Center, Case Western Reserve University, and the University of Texas at Dallas.

Declaration of competing interest

The authors declare that they have no known competing financial interests or personal relationships that could have appeared to influence the work reported in this paper.

Data availability

Data will be made available on request.

Acknowledgements

This work was supported in part by the National Institutes of Health, National Institute for Neurological Disorders and Stroke (R01NS110823, GRANT12635723, Capadona/Pancrazio) diversity supplement (Hernandez-Reynoso), and the National Institute for Biomedical Imaging and Bioengineering, (T32EB004314, Capadona/Kirsch). Also, this material is based upon work supported by the National Science Foundation Graduate Research Fellowship (Grant No. 1937968, Krebs). Additional support was provided by Merit Review Award (GRANT12418820, Capadona) and a Senior Research Career Scientist Award (GRANT12635707, Capadona) from the United States (US) Department of Veterans Affairs Rehabilitation Research and Development Service. The authors thank Dr. Alexandra Joshi-Imre and Dr. Negar Geramifard for the fabrication of non-functional devices for implantation. Data is available upon request to corresponding author.

Appendix A. Supplementary data

Supplementary data to this article can be found online at https://doi.org/10.1016/j.biomaterials.2023.122351.

References

[1] N. Fatima, A. Shuaib, M. Saqqur, Intra-cortical brain-machine interfaces for controlling upper-limb powered muscle and robotic systems in spinal cord injury, Clin. Neurol. Neurosurg. 196 (2020), 106069.
[2] Z.T. Irwin, K.E. Schroeder, P.P. Vu, A.J. Bullard, D.M. Tat, C.S. Nu, A. Vaskov, S. R. Nason, D.E. Thompson, J.N. Bentley, P.G. Patil, C.A. Chestek, Neural control of finger movement via intracortical brain–machine interface, J. Neural. Eng. 14 (6) (2017), 066004.
[3] C. Pandarinath, P. Nuyujukian, C.H. Blabe, B.L. Sorice, J. Saab, F.R. Willett, L. R. Hochberg, K.V. Shenoy, J.M. Henderson, High performance communication by people with paralysis using an intracortical brain-computer interface, Elife 6 (2017), e18554.
[4] A.C. Paulk, Y. Kfir, A.R. Khanna, M.L. Mustroph, E.M. Trautmann, D.J. Soper, S. D. Stavisky, M. Welkenhuysen, B. Dutta, K.V. Shenoy, L.R. Hochberg, R. M. Richardson, Z.M. Williams, S.S. Cash, Large-scale neural recordings with single neuron resolution using Neuropixels probes in human cortex, Nat. Neurosci. 25 (2) (2022) 252–263.
[5] A.B. Rapeaux, T.G. Constandinou, Implantable brain machine interfaces: first-in-human studies, technology challenges and trends, Curr. Opin. Biotechnol. 72 (2021) 102–111.
[6] J.D. Simeral, S.P. Kim, M.J. Black, J.P. Donoghue, L.R. Hochberg, Neural control of cursor trajectory and click by a human with tetraplegia 1000 days after implant of an intracortical microelectrode array, J. Neural. Eng. 8 (2) (2011), 025027.
[7] F.R. Willett, D.T. Avansino, L.R. Hochberg, J.M. Henderson, K.V. Shenoy, High-performance brain-to-text communication via handwriting, Nature 593 (7858) (2021) 249–254.
[8] A. Khorasani, N. Heydari Beni, V. Shalchyan, M.R. Daliri, Continuous force decoding from local field potentials of the primary motor cortex in freely moving rats, Sci. Rep. 6 (1) (2016), 35238.
[9] Y.S. Park, G.R. Cosgrove, J.R. Madsen, E.N. Eskandar, L.R. Hochberg, S.S. Cash, W. Truccolo, Early detection of human epileptic seizures based on intracortical microelectrode array signals, IEEE Trans. Biomed. Eng. 67 (3) (2020) 817–831.
[10] K.E. Schroeder, C.A. Chestek, Intracortical brain-machine interfaces advance sensorimotor neuroscience, Front. Neurosci. 10 (2016).
[11] T.D.Y. Kozai, A.S. Jaquins-Gerstl, A.L. Vazquez, A.C. Michael, X.T. Cui, Brain tissue responses to neural implants impact signal sensitivity and intervention strategies, ACS Chem. Neurosci. 6 (1) (2015) 48–67.
[12] N.F. Nolta, M.B. Christensen, P.D. Crane, J.L. Skousen, P.A. Tresco, BBB leakage, astrogliosis, and tissue loss correlate with silicon microelectrode array recording performance, Biomaterials 53 (2015) 753–762.
[13] K.A. Potter, A.C. Buck, W.K. Self, J.R. Capadona, Stab injury and device implantation within the brain results in inversely multiphasic neuroinflammatory and neurodegenerative responses, J. Neural. Eng. 9 (4) (2012), 046020.
[14] T. Saxena, L. Karumbaiah, E.A. Gaupp, R. Patkar, K. Patil, M. Betancur, G. B. Stanley, R.V. Bellamkonda, The impact of chronic blood–brain barrier breach on intracortical electrode function, Biomaterials 34 (20) (2013) 4703–4713.
[15] S.M. Wellman, T.D.Y. Kozai, In vivo spatiotemporal dynamics of NG2 glia activity caused by neural electrode implantation, Biomaterials 164 (2018) 121–133.
[16] E.S. Ereifej, G.M. Rial, J.K. Hermann, C.S. Smith, S.M. Meade, J.M. Rayyan, K. Chen, H. Feng, J.R. Capadona, Implantation of neural probes in the brain elicits oxidative stress, Front. Bioeng. Biotechnol. 6 (2018) 9.
[17] C. Bennett, F. Mohammed, A. Alvarez-Ciara, M.A. Nguyen, W.D. Dietrich, S. M. Rajguru, W.J. Streit, A. Prasad, Neuroinflammation, oxidative stress, and blood-brain barrier (BBB) disruption in acute Utah electrode array implants and the effect of deferoxamine as an iron chelator on acute foreign body response, Biomaterials 188 (2019) 144–159.
[18] J.S. Beckman, W.H. Koppenol, Nitric oxide, superoxide, and peroxynitrite: the good, the bad, and the ugly, Am. Phys. Soc. 271 (5 Pt 1) (1996) C1424–C1437.
[19] K.A. Potter-Baker, J.R. Capadona, Reducing the "stress": antioxidative therapeutic and material approaches may prevent intracortical microelectrode failure, ACS Macro Lett. 4 (3) (2015) 275–279.
[20] P. Takmakov, K. Ruda, K.S. Phillips, I.S. Isayeva, V. Krauthamer, C.G. Welle, Rapid evaluation of the durability of cortical neural implants using accelerated aging with reactive oxygen species, J. Neural. Eng. 12 (2) (2015), 026003.
[21] A. Contestabile, Oxidative stress in neurodegeneration: mechanisms and therapeutic perspectives, Curr. Top. Med. Chem. 1 (6) (2001) 553–568.
[22] D. Gallego, M. Rojas, C. Orozco, Free Radicals, Neuronal Death and Neuroprotection, Neurodegenerative Diseases-Processes, Prevention, Protection and Monitoring, IntechOpen2011.
[23] K. Chen, S.M. Wellman, Y. Yaxiaer, J.R. Eles, T.D.Y. Kozai, In vivo spatiotemporal patterns of oligodendrocyte and myelin damage at the neural electrode interface, Biomaterials 268 (2021), 120526-120526.
[24] G. Buzsáki, Large-scale recording of neuronal ensembles, Nat. Neurosci. 7 (5) (2004) 446–451.
[25] D.A. Henze, Z. Borhegyi, J. Csicsvari, A. Mamiya, K.D. Harris, G. Buzsáki, Intracellular features predicted by extracellular recordings in the Hippocampus in vivo, J. Neurophysiol. 84 (1) (2000) 390–400.
[26] R.S. Oakes, M.D. Polei, J.L. Skousen, P.A. Tresco, An astrocyte derived extracellular matrix coating reduces astrogliosis surrounding chronically implanted microelectrode arrays in rat cortex, Biomaterials 154 (2018) 1–11.
[27] A.J. Sawyer, W. Tian, J.K. Saucier-Sawyer, P.J. Rizk, W.M. Saltzman, R. V. Bellamkonda, T.R. Kyriakides, The effect of inflammatory cell-derived MCP-1 loss on neuronal survival during chronic neuroinflammation, Biomaterials 35 (25) (2014) 6698–6706.
[28] N. Kushwah, K. Woeppel, V. Dhawan, D. Shi, X.T. Cui, Effects of neuronal cell adhesion molecule L1 and nanoparticle surface modification on microglia, Acta Biomater. 149 (2022) 273–286.
[29] K.A. Potter, A.C. Buck, W.K. Self, M.E. Callanan, S. Sunil, J.R. Capadona, The effect of resveratrol on neurodegeneration and blood brain barrier stability surrounding intracortical microelectrodes, Biomaterials 34 (29) (2013) 7001–7015.
[30] K.A. Potter, M. Jorfi, K.T. Householder, E.J. Foster, C. Weder, J.R. Capadona, Curcumin-releasing mechanically adaptive intracortical implants improve the proximal neuronal density and blood–brain barrier stability, Acta Biomater. 10 (5) (2014) 2209–2222.
[31] K.A. Potter-Baker, W.G. Stewart, W.H. Tomaszewski, C.T. Wong, W.D. Meador, N. P. Ziats, J.R. Capadona, Implications of chronic daily anti-oxidant administration on the inflammatory response to intracortical microelectrodes, J. Neural. Eng. 12 (4) (2015), 046002.
[32] G.F. Hoeferlin, T. Bajwa, H. Olivares, J. Zhang, L.N. Druschel, B.S. Sturgill, M. Sobota, P. Boucher, J. Duncan, A.G. Hernandez-Reynoso, S.F. Cogan, J. J. Pancrazio, J.R. Capadona, Antioxidant Dimethyl Fumarate Temporarily but Not Chronically Improves Intracortical Microelectrode Performance, Micromachines 14 (10) (2023) 1902.

[33] R. Chen, J.L. Funnell, G.B. Quinones, M. Bentley, J.R. Capadona, R.J. Gilbert, E. F. Palermo, Poly(pro-curcumin) materials exhibit dual release rates and prolonged antioxidant activity as thin films and self-assembled particles, Biomacromolecules 24 (1) (2023) 294–307.

[34] A.M. Ziemba, M.C.C. Woodson, J.L. Funnell, D. Wich, B. Balouch, D. Rende, D. N. Amato, J. Bao, I. Oprea, D. Cao, N. Bajalo, E.S. Ereifej, J.R. Capadona, E. F. Palermo, R.J. Gilbert, Development of a slow-degrading polymerized curcumin coating for intracortical microelectrodes, ACS Appl. Bio Mater. 6 (2) (2023) 806–818.

[35] K.A. Potter-Baker, J.K. Nguyen, K.M. Kovach, M.M. Gitomer, T.W. Srail, W. G. Stewart, J.L. Skousen, J.R. Capadona, Development of superoxide dismutase mimetic surfaces to reduce accumulation of reactive oxygen species for neural interfacing applications, J. Mater. Chem. B 2 (16) (2014) 2248–2258.

[36] C.Y. Cheung, S.J. McCartney, K.S. Anseth, Synthesis of polymerizable superoxide dismutase mimetics to reduce reactive oxygen species damage in transplanted biomedical devices, Adv. Funct. Mater. 18 (20) (2008) 3119–3126.

[37] D. Liu, Y. Shan, L. Valluru, F. Bao, Mn (III) tetrakis (4-benzoic acid) porphyrin scavenges reactive species, reduces oxidative stress, and improves functional recovery after experimental spinal cord injury in rats: comparison with methylprednisolone, BMC Neurosci. 14 (1) (2013) 23.

[38] I. Batinić-Haberle, S. Cuzzocrea, J.S. Rebouças, G. Ferrer-Sueta, E. Mazzon, R. Di Paola, R. Radi, I. Spasojević, L. Benov, D. Salvemini, Pure MnTBAP selectively scavenges peroxynitrite over superoxide: comparison of pure and commercial MnTBAP samples to MnTE-2-PyP in two models of oxidative stress injury, an SOD-specific Escherichia coli model and carrageenan-induced pleurisy, Free Radic. Biol. Med. 46 (2) (2009) 192–201.

[39] P.S. Hume, K.S. Anseth, Polymerizable superoxide dismutase mimetic protects cells encapsulated in poly(ethylene glycol) hydrogels from reactive oxygen species-mediated damage, J. Biomed. Mater. Res. 99 (1) (2011) 29–37.

[40] S.M. Cy Cheung, K.S. Anseth, Synthesis of polymerizable superoxide dismutase mimetics to reduce reactive oxygen species damage in transplanted biomedical devices, Adv. Funct. Mater. 18 (2008) 3119–3126.

[41] O.K. Krebs, G. Mittal, S. Ramani, J. Zhang, A.J. Shoffstall, S.F. Cogan, J. J. Pancrazio, J.R. Au - Capadona, Tools for surface treatment of silicon planar intracortical microelectrodes, JoVE 184 (2022), e63500.

[42] W.-M. Munief, F. Heib, F. Hempel, X. Lu, M. Schwartz, V. Pachauri, R. Hempelmann, M. Schmitt, S. Ingebrandt, Silane deposition via gas-phase evaporation and high-resolution surface characterization of the ultrathin siloxane coatings, Langmuir 34 (35) (2018) 10217–10229.

[43] J.R. Capadona, D.M. Collard, A.J. García, Fibronectin adsorption and cell adhesion to mixed monolayers of tri(ethylene glycol)- and methyl-terminated alkanethiols, Langmuir 19 (5) (2003) 1847–1852.

[44] H.A. Hamedani, T. Stegall, Y. Yang, H. Wang, A. Menon, A. Bhalotia, E. Karathanasis, J.R. Capadona, A. Hess-Dunning, Flexible Multifunctional Titania Nanotube Array Platform for Biological Interfacing, Materials Research Society Bulletin (Under Review).

[45] J.P. Harris, A.E. Hess, S.J. Rowan, C. Weder, C.A. Zorman, D.J. Tyler, J. R. Capadona, In vivo deployment of mechanically adaptive nanocomposites for intracortical microelectrodes, J. Neural. Eng. 8 (4) (2011), 046010.

[46] A.M. Stiller, J. Usoro, C.L. Frewin, V.R. Danda, M. Ecker, A. Joshi-Imre, K. C. Musselman, W. Voit, R. Modi, J.J. Pancrazio, B.J. Black, Chronic intracortical recording and electrochemical stability of thiol-ene/acrylate shape memory polymer electrode arrays, Micromachines 9 (10) (2018).

[47] B. Sturgill, R. Radhakrishna, T.T. Thai, S.S. Patnaik, J.R. Capadona, J. J. Pancrazio, Characterization of active electrode yield for intracortical arrays: awake versus anesthesia, Micromachines 13 (3) (2022).

[48] J.O. Usoro, K. Dogra, J.R. Abbott, R. Radhakrishna, S.F. Cogan, J.J. Pancrazio, S. S. Patnaik, Influence of implantation depth on the performance of intracortical probe recording sites, Micromachines 12 (10) (2021).

[49] T.D.Y. Kozai, T.C. Marzullo, F. Hooi, N.B. Langhals, A.K. Majewska, E.B. Brown, D.R. Kipke, Reduction of neurovascular damage resulting from microelectrode insertion into the cerebral cortex using in vivo two-photon mapping, J. Neural. Eng. 7 (4) (2010).

[50] Y. Kim, E.S. Ereifej, W.E. Schwartzman, S.M. Meade, K. Chen, J. Rayyan, H. Feng, V. Aluri, N.N. Mueller, R. Bhambra, S. Bhambra, D.M. Taylor, J.R. Capadona, Investigation of the feasibility of ventricular delivery of resveratrol to the microelectrode tissue interface, Micromachines 12 (12) (2021).

[51] J.K. Nguyen, M. Jorfi, K.L. Buchanan, D.J. Park, E.J. Foster, D.J. Tyler, S. J. Rowan, C. Weder, J.R. Capadona, Influence of resveratrol release on the tissue response to mechanically adaptive cortical implants, Acta Biomater. 29 (2016) 81–93.

[52] T.B.G.F. Hoeferlin, H. Olivares, J. Zhang, L.N. Druschel, B. Sturgill, M. Sobota, P. Boucher, J. Duncan, A.G. Hernandez-Reynoso, S.F. Cogan, J.J. Pancrazio, J. R. Capadona, Antioxidant Dimethyl Fumarate Temporarily but Not Chronically Improves Microelectrode Performance, Micromachines Under Review, 2023.

[53] K.A. Potter, J.S. Simon, B. Velagapudi, J.R. Capadona, Reduction of autofluorescence at the microelectrode–cortical tissue interface improves antibody detection, J. Neurosci. Methods 203 (1) (2012) 96–105.

[54] H.W. Bedell, J.K. Hermann, M. Ravikumar, S. Lin, A. Rein, X. Li, E. Molinich, P. Smith, S. Sidik, D.M. Taylor, J.R. Capadona, Targeting CD14 on blood derived cells improves intracortical microelectrode performance, Biomaterials 163 (2018) 163–173.

[55] E.S. Ereifej, C.S. Smith, S.M. Meade, K. Chen, H. Feng, J.R. Capadona, The neuroinflammatory response to nanopatterning parallel grooves into the surface structure of intracortical microelectrodes, Adv. Funct. Mater. 28 (12) (2018), 1704420.

[56] J.K. Nguyen, M. Jorfi, K.L. Buchanan, D.J. Park, E.J. Foster, D.J. Tyler, S. J. Rowan, C. Weder, J.R. Capadona, Influence of resveratrol release on the tissue response to mechanically adaptive cortical implants, Acta Biomater. 29 (2016) 81–93.

[57] S.C. Lindner, M. Yu, J.R. Capadona, A.J. Shoffstall, A graphical user interface to assess the neuroinflammatory response to intracortical microelectrodes, J. Neurosci. Methods 317 (2019) 141–148.

[58] S. Song, L.N. Druschel, R. Chan, J.R. Capadona, Differential Expression of Genes Involved in the Chronic Response to Intracortical Microelectrodes Acta Biomaterialia under Review, 2023.

[59] H.W.B.S. Song, B.J. Regan, E.S. Ereifej, R. Chan, J.R. Capadona, Neuroinflammatory gene expression analysis reveals pathways of interest as potential targets to improve the recording performance of intracortical microelectrodes, Cells 11 (15) (2022) 2348.

[60] H.W. Bedell, N.J. Schaub, J.R. Capadona, E.S. Ereifej, Differential expression of genes involved in the acute innate immune response to intracortical microelectrodes, Acta Biomater. 102 (2020) 205–219.

[61] E.S. Ereifej, G. Rial, J.K. Hermann, C.S. Smith, S. Meade, J. Rayyan, K. Chen, H. Feng, J.R. Capadona, Implantation of neural probes in the brain elicits oxidative stress, Front. Bioeng. Biotechnol. 6 (9) (2018) 1–12.

[62] J.O. Usoro, B.S. Sturgill, K.C. Musselman, J.R. Capadona, J.J. Pancrazio, Intracortical microelectrode array unit yield under chronic conditions: a comparative evaluation, Micromachines 12 (8) (2021).

[63] K.B. Naoki Yamawaki, Benjamin A. Suter, Kenneth D. Harris, Gordon M. G. Shepherd, A genuine layer 4 in motor cortex with prototypical synaptic circuit connectivity, Elife 3 (2014), e05422.

[64] R. Biran, D.C. Martin, P.A. Tresco, Neuronal cell loss accompanies the brain tissue response to chronically implanted silicon microelectrode arrays, Exp. Neurol. 195 (1) (2005) 115–126.

[65] S.D. Skaper, The brain as a target for inflammatory processes and neuroprotective strategies, Ann. N. Y. Acad. Sci. 1122 (2007) 23–34.

[66] K.A. Potter, A.C. Buck, W.K. Self, J.R. Capadona, Stab injury and device implantation within the brain results in inversely multiphasic neuroinflammatory and neurodegenerative responses, J. Neural. Eng. 9 (4) (2012), 046020.

[67] Y. Xie, N. Martini, C. Hassler, R.D. Kirch, T. Stieglitz, A. Seifert, U.G. Hofmann, Frontiers in neuroengineering 7, in: Vivo Monitoring of Glial Scar Proliferation on Chronically Implanted Neural Electrodes by Fiber Optical Coherence Tomography, 2014.

[68] J.O. Usoro, B.S. Sturgill, K.C. Musselman, J.R. Capadona, J.J. Pancrazio, Intracortical microelectrode array unit yield under chronic conditions: a comparative evaluation, Micromachines 12 (8) (2021).

[69] C.J. Barnett J, D. Ives, M. Chiou, R. Mackenzie, E. Osen, B. Nguyen, S. Tsing, C. Bach, J. Freire, et al., Purification, characterization and selective inhibition of human prostaglandin G/H synthase 1 and 2 expressed in the baculovirus system, Biochim. Biophys. Acta 1209 (1) (1994) 130–139.

[70] H.A. Neubert P, D. Wendelborn, A.L. Bär, L. Krampert, M. Trum, A. Schröder, S. Ebner, A. Weichselbaum, V. Schatz, P. Linz, R. Veelken, J. Schulte-Schrepping, A.C. Aschenbrenner, T. Quast, C. Kurts, S. Geisberger, K. Kunzelmann, K. Hammer, K.J. Binger, J. Titze, D.N. Müller, W. Kolanus, J.L. Schultze, S. Wagner, J. Jantsch, NCX1 represents an ionic Na+ sensing mechanism in macrophages, PLoS Biol. 18 (6) (2020).

[71] C.X. Zhou Y, Y. Yang, J. Wang, W. Yang, P. Ben, L. Shen, P. Cao, L. Luo, Z. Yin, Glutathione S-transferase Pi prevents sepsis-related high mobility group box-1 protein translocation and release, Front. Immunol. 9 (268) (2018).

[72] L. Luo, Y. Wang, Q. Feng, H. Zhang, B. Xue, J. Shen, Y. Ye, X. Han, H. Ma, J. Xu, D. Chen, Z. Yin, RecombinantproteinglutathioneS-transferasesP1attenuates inflammationinmice, Mol. Immunol. 46 (2009) 848–857.

[73] K.M. Rothgiesser, S. Erener, S. Waibel, B. Lüscher, M.O. Hottiger, SIRT2 regulates NF-κB-dependent gene expression through deacetylation of p65 Lys310, J. Cell Sci. 123 (24) (2010) 4251–4258.

[74] R. Pandithage, R. Lilischkis, K. Harting, A. Wolf, B. Jedamzik, J. LuScher-Firzlaff, J.R. Vervoorts, E. Lasonder, E. Kremmer, B. KnoLl, B. LuScher, The regulation of SIRT2 function by cyclin-dependent kinases affects cell motility, J. Cell Biol. 180 (5) (2008) 915–929.

[75] S.-G. Jeong, G.-W. Cho, The tubulin deacetylase sirtuin-2 regulates neuronal differentiation through the ERK/CREB signaling pathway, Biochem. Biophys. Res. Commun. 482 (1) (2017) 182–187.

[76] M. Jorfi, K.A. Potter, J.K. Nguyen, A.E. Hess-Dunning, E.J. Foster, J.R. Capadona, C. Weder, Mechanically Adaptive Materials for Intracortical Implants, 2015 7th International IEEE/EMBS Conference on Neural Engineering, IEEE, 2015, pp. 601–602.

[77] D. Davalos, J. Grutzendler, G. Yang, J.V. Kim, Y. Zuo, S. Jung, D.R. Littman, M. L. Dustin, W.-B. Gan, ATP mediates rapid microglial response to local brain injury in vivo, Nat. Neurosci. 8 (6) (2005) 752–758.

[78] A. Nimmerjahn, F. Kirchhoff, F. Helmchen, Resting microglial cells are highly dynamic surveillants of brain parenchyma in vivo, Science 308 (5726) (2005) 1314–1318.

[79] H.W. Bedell, S. Song, X. Li, E. Molinich, S. Lin, A. Stiller, V. Danda, M. Ecker, A. J. Shoffstall, W.E. Voit, J.J. Pancrazio, J.R. Capadona, Understanding the effects of both CD14-mediated innate immunity and device/tissue mechanical mismatch in the neuroinflammatory response to intracortical microelectrodes, Front. Neurosci. 12 (2018).

[80] J.W. Salatino, K.A. Ludwig, T.D.Y. Kozai, E.K. Purcell, Glial responses to implanted electrodes in the brain, Nat. Biomed. Eng. 1 (11) (2017) 862–877.

[81] C.M. Atkins, J.D. Sweatt, Reactive oxygen species mediate activity-dependent neuron-glia signaling in output fibers of the hippocampus, J. Neurosci. 19 (17) (1999) 7241–7248.
[82] U. Pannasch, N. Rouach, Emerging role for astroglial networks in information processing: from synapse to behavior, Trends Neurosci. 36 (7) (2013) 405–417.
[83] K.A. Guttenplan, B.K. Stafford, R.N. El-Danaf, D.I. Adler, A.E. Münch, M. K. Weigel, A.D. Huberman, S.A. Liddelow, Neurotoxic reactive astrocytes drive neuronal death after retinal injury, Cell Rep. 31 (12) (2020), 107776.
[84] P.A. Schwartzkroin, S.C. Baraban, D.W. Hochman, Osmolarity, ionic flux, and changes in brain excitability, Epilepsy Res. 32 (1–2) (1998) 275–285.
[85] K. Oyarce, M.Y. Cepeda, R. Lagos, C. Garrido, A.M. Vega-Letter, M. Garcia-Robles, P. Luz-Crawford, R. Elizondo-Vega, Neuroprotective and neurotoxic effects of glial-derived exosomes, Front. Cell. Neurosci. 16 (2022).
[86] Y. You, K. Borgmann, V.V. Edara, S. Stacy, A. Ghorpade, T. Ikezu, Activated human astrocyte-derived extracellular vesicles modulate neuronal uptake, differentiation and firing, J. Extracell. Vesicles 9 (1) (2020), 1706801.
[87] M.D. Johnson, K.J. Otto, D.R. Kipke, Repeated voltage biasing improves unit recordings by reducing resistive tissue impedances, IEEE Trans. Neural Syst. Rehabil. Eng. 13 (2) (2005) 160–165.
[88] L.J. Szymanski, S. Kellis, C.Y. Liu, K.T. Jones, R.A. Andersen, D. Commins, B. Lee, D.B. McCreery, C.A. Miller, Neuropathological effects of chronically implanted, intracortical microelectrodes in a tetraplegic patient, J. Neural. Eng. 18 (4) (2021), 0460b9-0460b9.
[89] P.A. Cody, J.R. Eles, C.F. Lagenaur, T.D.Y. Kozai, X.T. Cui, Unique electrophysiological and impedance signatures between encapsulation types: an analysis of biological Utah array failure and benefit of a biomimetic coating in a rat model, Biomaterials 161 (2018) 117–128.
[90] K.A. Malaga, K.E. Schroeder, P.R. Patel, Z.T. Irwin, D.E. Thompson, J. Nicole Bentley, S.F. Lempka, C.A. Chestek, P.G. Patil, Data-driven model comparing the effects of glial scarring and interface interactions on chronic neural recordings in non-human primates, J. Neural. Eng. 13 (1) (2015).
[91] A. Prasad, J.C. Sanchez, Quantifying long-term microelectrode array functionality using chronic in vivo impedance testing, J. Neural. Eng. 9 (2) (2012), 026028.
[92] S.M. Wellman, K. Guzman, K.C. Stieger, L.E. Brink, S. Sridhar, M.T. Dubaniewicz, L. Li, F. Cambi, T.D.Y. Kozai, Cuprizone-induced oligodendrocyte loss and demyelination impairs recording performance of chronically implanted neural interfaces, Biomaterials 239 (2020), 119842-119842.
[93] D.S.A. Simpson, P.L. Oliver, ROS generation in microglia: understanding oxidative stress and inflammation in neurodegenerative disease, Antioxidants 9 (8) (2020).
[94] Y. Chen, C. Qin, J. Huang, X. Tang, C. Liu, K. Huang, J. Xu, G. Guo, A. Tong, L. Zhou, The role of astrocytes in oxidative stress of central nervous system: a mixed blessing, Cell Prolif. 53 (3) (2020), e12781.
[95] V.V. Gusel'nikova, D.E. Korzhevskiy, NeuN as a neuronal nuclear antigen and neuron differentiation marker, Acta Naturae 7 (2) (2015) 42–47.
[96] A.S. Cort H Thompson, Nicholas Heelan, Salatino Joseph, Erin K. Purcell, Spatiotemporal patterns of gene expression around implanted silicon electrode arrays, J. Neural. Eng. 18 (4) (2021) 1741–2552.
[97] N.J. Michelson, A.L. Vazquez, J.R. Eles, J.W. Salatino, E.K. Purcell, J.J. Williams, X.T. Cui, T.D.Y. Kozai, Multi-scale, multi-modal analysis uncovers complex relationship at the brain tissue-implant neural interface: new emphasis on the biological interface, J. Neural. Eng. 15 (3) (2018), 033001.
[98] K. Joseph, M. Kirsch, M. Johnston, C. Munkel, T. Stieglitz, C.A. Haas, U. G. Hofmann, Transcriptional characterization of the glial response due to chronic neural implantation of flexible microprobes, Biomaterials 279 (2021), 121230.
[99] A.J. Shoffstall, J.E. Paiz, D.M. Miller, G.M. Rial, M.T. Willis, D.M. Menendez, S. R. Hostler, J.R. Capadona, Potential for thermal damage to the blood–brain barrier during craniotomy: implications for intracortical recording microelectrodes, J. Neural. Eng. 15 (3) (2018), 034001.
[100] G.F. Hoeferlin, D.M. Menendez, O.K. Krebs, J.R. Capadona, A.J. Shoffstall, Assessment of thermal damage from robot-drilled craniotomy for cranial window surgery in Mice, JoVE 189 (2022), e64188.
[101] C. Bennett, M. Samikkannu, F. Mohammed, W.D. Dietrich, S.M. Rajguru, A. Prasad, Blood brain barrier (BBB)-disruption in intracortical silicon microelectrode implants, Biomaterials 164 (2018) 1–10.
[102] G.C. McConnell, H.D. Rees, A.I. Levey, C.-A.A. Gutekunst, R.E. Gross, R. V. Bellamkonda, Implanted neural electrodes cause chronic, local inflammation that is correlated with local neurodegeneration, J. Neural. Eng. 6 (5) (2009), 56003-56003.
[103] K. Biswas, K. Alexander, M.M. Francis, Reactive oxygen species: angels and demons in the life of a neuron, NeuroSci. 3 (1) (2022) 130–145.
[104] M.J. O'Connell, H. Baum, T.J. Peters, Haemosiderin-like properties of free-radical-modified ferritin, Biochem. J. 240 (1) (1986) 297–300.
[105] M. Ravikumar, S. Sunil, J. Black, D.S. Barkauskas, A.Y. Haung, R.H. Miller, S. M. Selkirk, J.R. Capadona, The roles of blood-derived macrophages and resident microglia in the neuroinflammatory response to implanted Intracortical microelectrodes, Biomaterials 35 (28) (2014) 8049–8064.
[106] T.Y. Chang, V.G. Yadav, S. De Leo, A. Mohedas, B. Rajalingam, C.-L. Chen, S. Selvarasah, M.R. Dokmeci, A. Khademhosseini, Cell and protein compatibility of Parylene-C surfaces, Langmuir 23 (23) (2007) 11718–11725.
[107] G. Valette, Hydrophilicity of metal surfaces: silver, gold and copper electrodes, J. Electroanal. Chem. Interfacial Electrochem. 139 (2) (1982) 285–301.
[108] L. Chen, X. He, H. Liu, L. Qian, S.H. Kim, Water adsorption on hydrophilic and hydrophobic surfaces of silicon, J. Phys. Chem. C 122 (21) (2018) 11385–11391.
[109] A. Prasad, Q. Xue, V. Sankar, T. Nishida, G. Shaw, W. Streit, J.C. Sanchez, Comprehensive characterization of tungsten microwires in chronic neurocortical implants, in: 2012 Annual International Conference of the IEEE Engineering in Medicine and Biology Society, 2012, pp. 755–758.
[110] T.D.Y. Kozai, X. Li, L.M. Bodily, E.M. Caparosa, G.A. Zenonos, D.L. Carlisle, R. M. Friedlander, X.T. Cui, Effects of caspase-1 knockout on chronic neural recording quality and longevity: insight into cellular and molecular mechanisms of the reactive tissue response, Biomaterials 35 (36) (2014) 9620–9634.
[111] I. Ünal-Çevik, M. Kılınç, Y. Gürsoy-Özdemir, G. Gurer, T. Dalkara, Loss of NeuN immunoreactivity after cerebral ischemia does not indicate neuronal cell loss: a cautionary note, Brain Res. 1015 (1) (2004) 169–174.
[112] V.V. Gusel'nikova, D.E. Korzhevskiy, NeuN as a neuronal nuclear antigen and neuron differentiation marker, Acta Naturae 7 (2075–8251) (2015) 42–47.
[113] C.H. Thompson, A. Saxena, N. Heelan, J. Salatino, E.K. Purcell, Spatiotemporal patterns of gene expression around implanted silicon electrode arrays, J. Neural. Eng. 18 (4) (2021), 045005.
[114] G.R. Chichili, D. Nohr, J. Frank, A. Flaccus, P.D. Fraser, E.M.A. Enfissi, H. K. Biesalski, Protective effects of tomato extract with elevated β-carotene levels on oxidative stress in ARPE-19 cells, Br. J. Nutr. 96 (4) (2006) 643–649.
[115] T.D.Y. Kozai, K. Catt, X. Li, Z.V. Gugel, V.T. Olafsson, A.L. Vazquez, X.T. Cui, Mechanical failure modes of chronically implanted planar silicon-based neural probes for laminar recording, Biomaterials 37 (2015) 25–39.
[116] B.J. Black, A. Kanneganti, A. Joshi-Imre, R. Rihani, B. Chakraborty, J. Abbott, J. J. Pancrazio, S.F. Cogan, Chronic recording and electrochemical performance of Utah microelectrode arrays implanted in rat motor cortex, J. Neurophysiol. 120 (4) (2018) 2083–2090.
[117] J.C. Barrese, J. Aceros, J.P. Donoghue, Scanning electron microscopy of chronically implanted intracortical microelectrode arrays in non-human primates, J. Neural. Eng. 13 (2) (2016), 026003.
[118] X.S. Zheng, N.R. Snyder, K. Woeppel, J.H. Barengo, X. Li, J. Eles, C.L. Kolarcik, X. T. Cui, A superoxide scavenging coating for improving tissue response to neural implants, Acta Biomater. 99 (2019) 72–83.
[119] R.M. Haley, S.T. Zuckerman, H. Dakhlallah, J.R. Capadona, H.A. Von Recum, E. S. Ereifej, Resveratrol delivery from implanted cyclodextrin polymers provides sustained antioxidant effect on implanted neural probes, Int. J. Mol. Sci. 21 (10) (2020).